**Naval Research Laboratory**
Washington, DC 20375-5320

U.S. NAVAL RESEARCH LABORATORY

**NRL/6040/MR—2024/1**

# Simulations of Bio-Inspired Flexible Flapping Fins

RAVI RAMAMURTI

JASON GEDER

KAMAL VISWANATH

*Laboratory for Propulsion, Energetics and Dynamics Branch*
*Laboratory for Computational Physics and Fluid Dynamics Division*

PROF. RAINALD LÖHNER

*CFD Center*
*George Mason University*
*Fairfax, VA*

KAUSHIK SAMPATH

*KS Research, Inc.*
*Riverdale, MD*

April 5, 2024

# REPORT DOCUMENTATION PAGE

**PLEASE DO NOT RETURN YOUR FORM TO THE ABOVE ORGANIZATION**

| 1. REPORT DATE | 2. REPORT TYPE | 3. DATES COVERED | |
|---|---|---|---|
| | | START DATE | END DATE |
| 05-04-2024 | NRL Memorandum Report | October 2020 | December 2023 |

**4. TITLE AND SUBTITLE**
Simulations of Bio-Inspired Flexible Flapping Fins

| 5a. CONTRACT NUMBER | 5b. GRANT NUMBER | 5c. PROGRAM ELEMENT NUMBER |
|---|---|---|
| | | |
| **5d. PROJECT NUMBER** | **5e. TASK NUMBER** | **5f. WORK UNIT NUMBER** |
| | | 6C40 |

**6. AUTHOR(S)**
Ravi Ramamurti, Jason Geder, Kamal Viswanath, Prof. Rainald Löhner*, and Kaushik Sampath**

**7. PERFORMING ORGANIZATION / AFFILIATION NAME(S) AND ADDRESS(ES)**
Naval Research Laboratory, Washington, D.C. 20375,
George Mason University, Fairfax VA 22030, and
KS Research, Inc., Riverdale MD 20737

**8. PERFORMING ORGANIZATION REPORT NUMBER**
NRL/6040/MR—2024/1

| 9. SPONSORING / MONITORING AGENCY NAME(S) AND ADDRESS(ES) | 10. SPONSOR / MONITOR'S ACRONYM(S) NUMBER | 11. SPONSOR / MONITOR'S REPORT NUMBER(S) |
|---|---|---|
| Naval Research Laboratory<br>4555 Overlook Ave SW<br>Washington, DC 20375-5320 | NRL | |

**12. DISTRIBUTION / AVAILABILITY STATEMENT**
**DISTRIBUTION STATEMENT A:** Approved for public release; distribution is unlimited.

**13. SUPPLEMENTAL NOTES**
*CFD Center, George Mason University, Fairfax, VA 22030
**KS Research, Inc., Riverdale, MD 20737

**14. ABSTRACT**
A fluid structure interaction modeling tool developed for the simulation of thrust generation using flexible flapping wings is used to model flexible fins for Unmanned Underwater Vehicle applications. The coupled solver based on eigenmodes is used to model the flexible fins flapping in tandem separated by an axial offset. The effect of flexibility of the fin is studied using material of two different Young's moduli and compared with its rigid counterpart. Parametric studies were conducted varying the axial offset distance, the phase offset between the tandem fins and the flapping fin kinematics. Analysis shows that the flexibility of the fin and the phase offset play an important role in the thrust production of the rear fin. The data in terms of velocity and vorticity at several axial planes are provided to validate the experimentally obtained PIV flow results and to improve the understanding of these complex propulsive systems.

**15. SUBJECT TERMS**
Fluid dynamics, bio-inspiration, UUVs, flexible flapping fins.

| 16. SECURITY CLASSIFICATION OF: | | | 17. LIMITATION OF ABSTRACT | 18. NUMBER OF PAGES |
|---|---|---|---|---|
| a. REPORT | b. ABSTRACT | c. THIS PAGE | | |
| U | U | U | SAR | 32 |

| 19a. NAME OF RESPONSIBLE PERSON | 19b. PHONE NUMBER *(Include area code)* |
|---|---|
| Ravi Ramamurti | (202) 767-3640 |

This page intentionally left blank.

## Table of Contents



## List of Figures

# Simulations of Bio-Inspired Flexible Flapping Fins

## INTRODUCTION

In recent years, there has been increased experimental and analytical investigations of the biomechanics and hydrodynamics of fish propulsion for quantifying the propulsive performance of a variety of propulsive modes, see e.g. Lauder [1]. Fishes such as the bird-wrasse that swim with paired pectoral fins use fin stroke parameters that produce thrust force from lift in powering their underwater motion. Other fishes, such as the tuna and mackerels, produce thrust almost exclusively via oscillating caudal fin. Flapping locomotion mechanisms are of interest to behavioral biologists, biomechanics researchers, and engineers attempting to develop systems that can match the performance of the living creatures. In investigating the mechanisms responsible for the high force generation in flapping locomotion, the importance of the planform of the fins, the kinematics of the motion and interaction of the flow between various propulsive surfaces must be explored. While biologists and engineers have worked together to study and take inspiration from nature in the development of artificial flapping fins, research seeking to understand the propulsive performance of a system of multiple fins operating on a vehicle is limited.

There is a large body of literature by various research groups [3-6] on the study of fin shapes, strokes parameters, and configurations, as well as different fin materials. While there is a rich set of data covering many parameters for isolated fins, studies of the propulsive performance of a system of multiple fins are far less common. In order to create an effective tool for the design and analysis of vehicles propelled by artificial fins, more comprehensive studies to identify the effects of various fin parameters on the interactions between multiple fins is essential. The parametric space for designing a system of multiple flapping fins including the fin geometry, relative phasing and spacing between the fins, flexibility of the fins is quite large. The major aim of this research is to employ the recently developed modeling tool [7] for flexible fins to study the effect of flexibility of the fin on the propulsive forces for a multi-fin system and to develop a reduced order model.

## THE INCOMPRESSIBLE FLOW SOLVER

The governing equations employed are the incompressible Navier-Stokes equations in Arbitrary Lagrangian-Eulerian (ALE) formulation which are written as,

$$\rho \mathbf{v}_{,t} + \rho \mathbf{v}_a \nabla \mathbf{v} + \boldsymbol{\nabla} p = \nabla \mu \nabla \mathbf{v} \quad , \tag{1}$$

$$\nabla . \mathbf{v} = 0 \quad , \tag{2}$$

where $p$ denotes the pressure, $\mathbf{v}_a = \mathbf{v} - \mathbf{w}$ is the advective velocity vector, where $\mathbf{v}$ is the flow velocity and $\mathbf{w}$ is the mesh velocity and $\mu$ is the turbulent viscosity. Thus, the equations are Eulerian for zero mesh velocity and Lagrangian if the mesh velocity is the same as the flow velocity. The present time-accurate flow solver uses a spatial discretization based on a Galerkin procedure with linear tetrahedral elements, and a temporal discretization based on fractional steps for velocities and pressure. The details of the flow solver have already been discussed extensively elsewhere (Ramamurti et. al. [8-9]) in connection with successfully validated solutions for numerous 2-D and 3-D, laminar and turbulent, steady and unsteady flow problems.

Manuscript approved April 2, 2024.

**Coupling Structural Solver to CFD**

The coupling of the fluid flow and the elastic structural deformation can be carried out in two ways. The first method discretizes the structure using finite elements but assumes that only small elastic deformations occur. Based on the finite element model, a modal decomposition is carried out, and the eigenmodes of the structure are obtained. These eigenmodes are then coupled to the fluid solver. The second strategy involves discretizing the structure using finite elements and solving the structural deformation in a time-accurate manner based on the physical properties. Note that while in the first method only principal eigenmodes are used, in the second method all the eigenmodes that can be seen by the discretization are present, i.e., the maximum possible amount of information is used.

The discretization of the elastic structure via finite elements results in the system,

$$\mathbf{M}\ddot{\mathbf{w}} + \mathbf{D}\dot{\mathbf{w}} + \mathbf{K}\mathbf{w} = \mathbf{f} \quad , \tag{3}$$

where **M**, **D**, and **K** are the mass, damping and stiffness matrices, respectively, **w** is the vector of nodal displacement and **f** is the external force. The matrices **M** and **K** are symmetric positive definite, and can be used to obtain a system of eigenmodes by solving the eigenvalue problem,

$$(-\omega_i^2\mathbf{M} + \mathbf{K}) \cdot e^i = 0, \;\; i = 1, n \quad . \tag{4}$$

The vector of unknowns **w** can be written in terms of the eigenvectors as

$$\mathbf{w} = e^i a_i, \tag{5}$$

resulting in

$$\mathbf{M}e^i\ddot{a}_i + \mathbf{D}e^i\dot{a}_i + \mathbf{K}e^i a_i = \mathbf{f} \quad . \tag{6}$$

Assuming $e^j\mathbf{D}e^i = d^{ii}\delta^{ij}$, we can decompose Eq. (5) by multiplying with $e^j$, and using the orthogonality properties of **M** and **K**,

$$e^j\mathbf{M}e^i = \delta^{ij}, \text{ and } e^j\mathbf{K}e^i = \omega_i^2\delta^{ij} \quad , \tag{7}$$

where $\delta^{ij}$ is the Kronecker delta. This results in a decoupled system of ordinary differential equations

$$\ddot{a}_j + d^{jj}\dot{a}_j + \omega_j^2 a_j = f^j = \mathbf{f} \cdot e^j \quad . \tag{8}$$

This system of ODEs can be solved either given the forcing loads **f** resulting in the nodal displacement **w**, or given the motion $a_i$, resulting in the nodal displacement **w**. In some cases, the eigenvectors are not scaled according to Eq. (7). Instead, they are of the form

$$\boldsymbol{j}^i = \alpha^i e^i \quad , \tag{9}$$

and the nodal displacement **w** is written as

$$\mathbf{w} = \boldsymbol{j}^i b_i, \tag{10}$$

resulting in

$$\ddot{b}_i + d^{ii}\dot{b}_i + \omega_i^2 b_i = \frac{1}{(\alpha^i)^2}\mathbf{f} \cdot \boldsymbol{j}^i \quad . \tag{11}$$

The scaling factor $\alpha^i$ can be obtained by applying a known force and matching the corresponding displacements and is used as an input in coupling the modes with the CFD solver. If we consider beam elements, the basic equation is

$$\rho A\ddot{w} + EI\, w_{,xxxx} = q \quad , \tag{12}$$

where $w$ is the displacement, $\rho$ is the density, $A$ is the cross-sectional area of the beam, $E$ is the Young's modulus, $I$ is the area moment of the beam and $q$ is the force per unit length. The eigenfunctions for this system can be written as

$$w = w_0 w_s(\lambda x), \;\; w_{,xxxx} = \lambda^4 w \;\; . \tag{13}$$

Substituting this in Eq. (12) and applying a Galerkin approximation, we get

$$\rho A c_w \ddot{w}_0 + EI\lambda^4 c_w w_0 = \int q w_s(\lambda x)\, dx\,, \quad c_w = \int w_s^2(\lambda dx) dx \;\; . \tag{14}$$

The force integral can be approximated by point collocation as

$$\int q w_s(\lambda x)\, dx = \sum_i w_s(\lambda x_i)\, F(x_i) \;\; , \tag{15}$$

resulting in the following eigenmode system

$$m\ddot{w} + kw = \sum_i w_s(\lambda x_i)\, F(x_i) \;\; , \tag{16}$$

where $m = \rho A c_w$, and $k = EI\lambda^4 c_w$. For different boundary conditions, such as cantilevered beam and free beams, the eigenvalues can be found from standard test books. These are used to validate the coupled solver.

## APPLICATION OF THE COUPLED MODEL

The coupled eigenmode model described above was validated for the 2-D beam problem and compared with the benchmark solution of Turek-Hron [10]. This model was applied to the 3-D flapping fin developed for UUVs. The planform for the fins is based on previous research [11] is a bio-inspired trapezoidal fin, Fig.1.

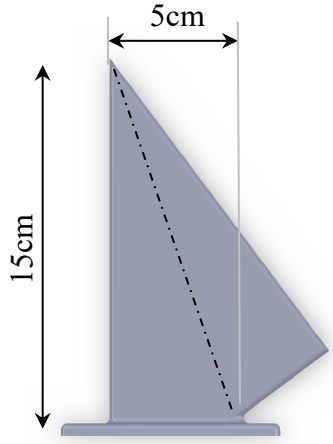


Fig. 1. Planform of a bio-inspired fin of aspect ratio 3.

### *Tandem flapping fin setup:*

For these studies, we selected a two-fin system sharing the stroke rotation axis and separated by an axial offset distance, $x_{offset}$, in the axial direction, as shown in Fig. 2a. In order to study the effect of the phasing between the front and rear stroke angles, the rear fin is offset by a fraction of the stroke amplitude, $\delta$, defined as

$$\delta = \frac{\phi_{offset}}{\Phi} 180° \tag{17}$$

where $\phi_{offset}$ is the phase offset between the front and rear fins and Φ is the stroke amplitude of the fin shown in Fig. 2b. In this study, two axial offsets of 12cm and 15cm, and several phase offsets between ±180° are considered. The stroke rotation axis is set at 3.175cm from the base of the fin. The kinematics used for the pitch rotation and angle of attack of the fin are shown in Fig. 3. This kinematics was used in the earlier studies with the rigid fin, and has a stroke amplitude of 58° and a pitch amplitude 38°.

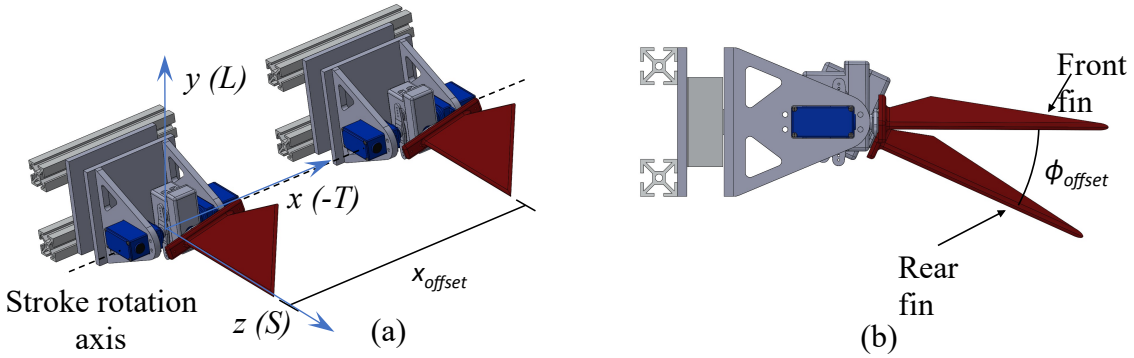


Fig. 2. Tandem fin system showing (a) the stroke rotation axis and the axial offset and (b) the stroke phase offset between the front and rear fins.

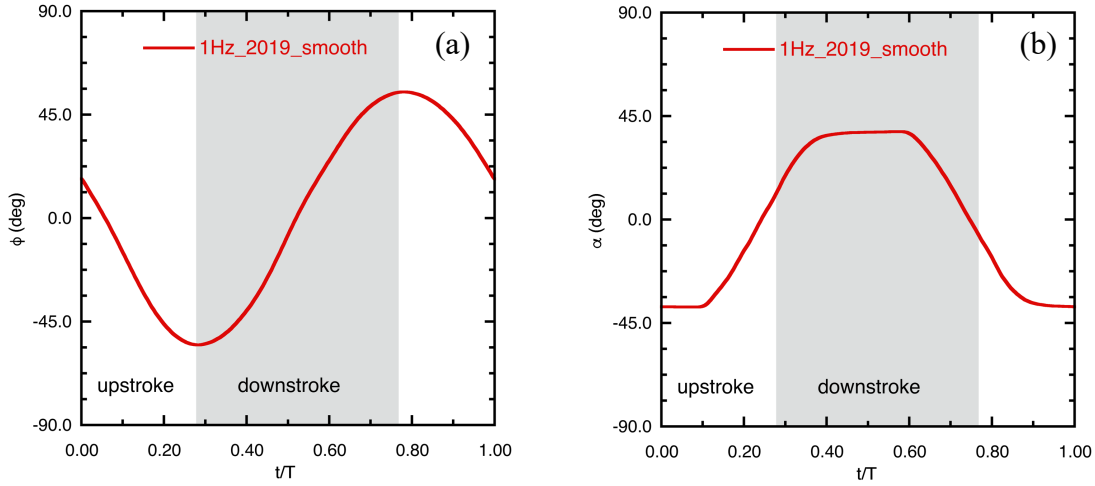


Fig. 3. Kinematics of the flapping fin, (a) stroke angle and (b) pitch angle, $f$ = 1Hz.

In order to obtain the eigenmodes of the flexible fin, the fin is decomposed into 2 regions, a rigid leading edge and a flexible trailing edge region, as shown in Fig. 4. The rigid region in the experiment contains a spar and the flexible portion is made up of PDMS material. The rigid section is made up of a material with a Young's modulus, E = 1.7 × $10^3$ MPa and the flexible material's is 0.75 MPa. The density of the rigid and the flexible materials are 930 Kg/$m^3$ and 970 Kg/$m^3$, and the Poisson's ratio $\nu$, are 0.4 and 0.49, respectively. The eigenmodes of the combined fin are next generated using COMSOL, using these material properties and the surface triangulation. The displacement for each of the modes at the surface points are used in the coupled solver.

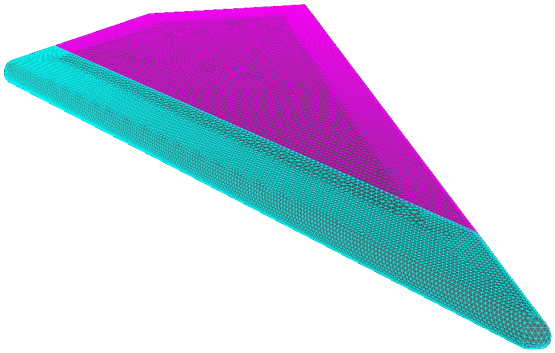

Fig. 4. Surface mesh of the flexible fin showing the rigid section (cyan) and the flexible section (magenta).

***Single Flapping fin:***

First, the coupled solver is validated for a single rigid fin flapping at 1Hz. The coupled solver uses an embedded mesh approach, where the fin is treated as an embedded body in the surrounding fluid. In our previous flapping fin simulations, we have used a body-fitted approach, wherein the moving fin is treated in an ALE formulation coupled with remeshing. In order to mimic a rigid fin, the number of eigenmode is set to zero. The fin surface consists of 62.1k points and 125k triangles, and the volume mesh for the embedded case consists of 3.08M points and 18.2M tetrahedral elements. Figure 5 shows the comparison of the thrust history between the two approaches, and shows the coupled embedded approach is able to reproduce previous result.

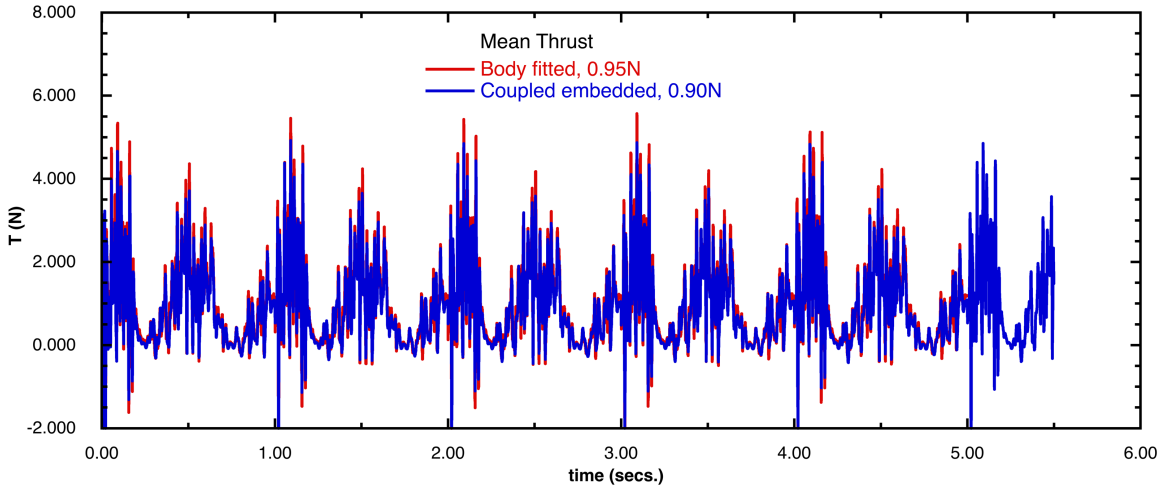


Fig. 5. Time history of the thrust for the rigid flapping fin, f = 1Hz.

Next, simulations were performed with the isolated flapping fin with all eigenmodes. The first 7 modes for a fin with E =0.75MPa, shown in Fig. 6, are used for this simulation. Using COMSOL, a steady displacement of the fin is obtained using a constant differential pressure of 1Pa between the top and bottom surfaces of the fin, shown in Fig. 7. The scaling factor $\alpha^i$ , Eq. 11, is then obtained to match this displacement. The time history of the thrust force with the flexible fin, Fig. 8, shows a mean thrust of 0.88N slightly reduced from the rigid fin's valued of 0.9N. During the simulation, the location of the leading and trailing edge tips, Fig. 9a, were monitored throughout the flapping cycle. The relative displacement of these points w.r.to the rigid

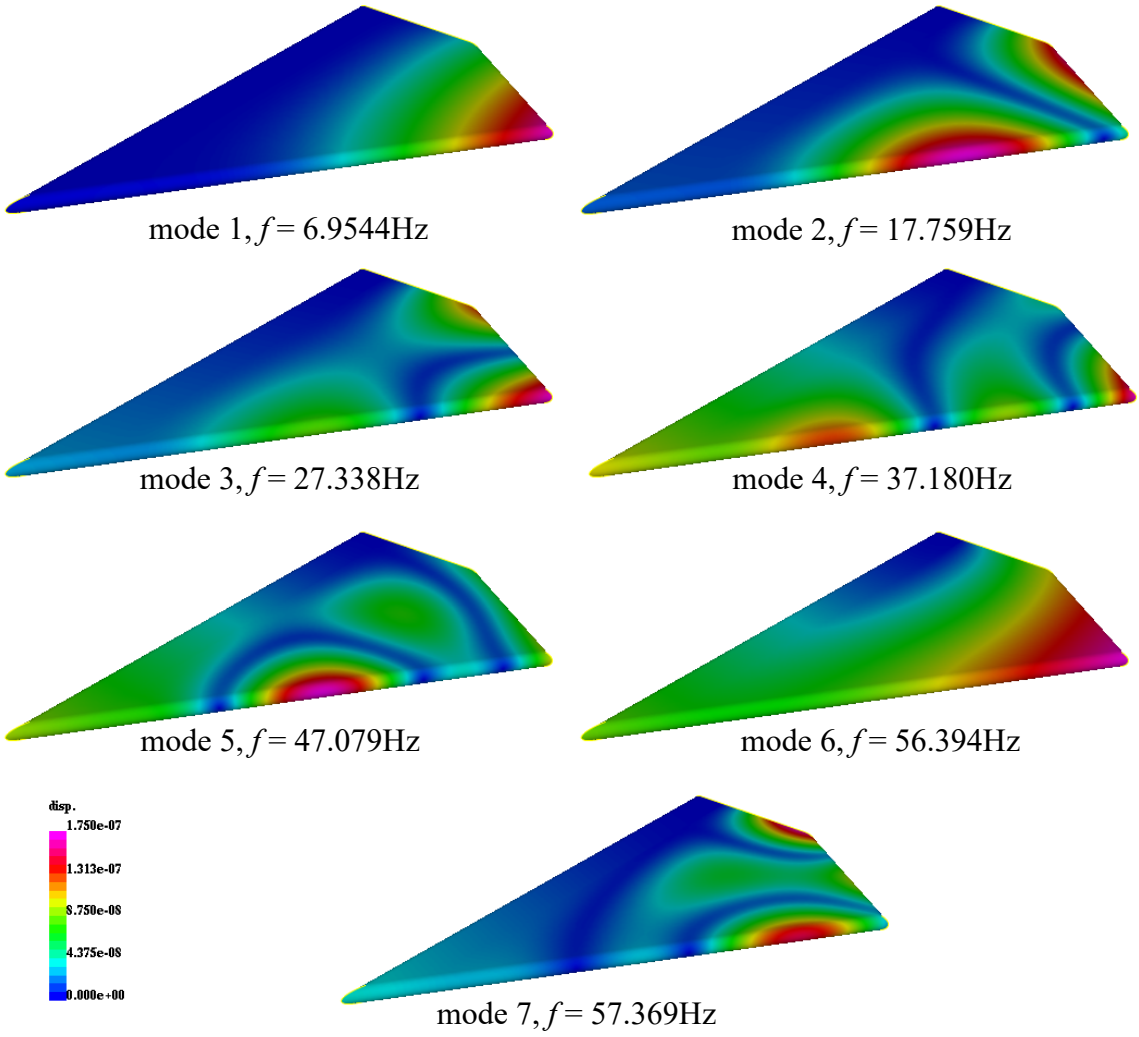


Fig. 6. Eigenmodes for the flexible fin, $E$ = 0.75MPa.

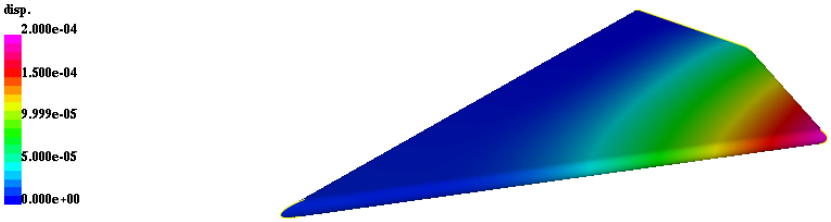


Fig. 7. Steady displacement of the fin with a differential pressure of 1Pa.

rotations are shown in Fig. 9b. The leading edge tip excursion is within 10% of the chord due to the rigid nature of the material and the trailing edge reached close to 60% of the chord.

***Tandem Flapping fins separated by 15cm:***

*Pitch amplitude 18°, f= 1Hz:*

The coupled approach is then applied to tandem flapping fins, separated by 15cm. The kinematics for this simulation is shown in Fig. 10, and has a stroke amplitude of 61° and a pitch

amplitude, $\alpha_{0,}$ of 18°. Similar set of kinematics was used to validate the shape of the flexible flapping fin and was shown to be in good agreement with the experimental results [12]. The

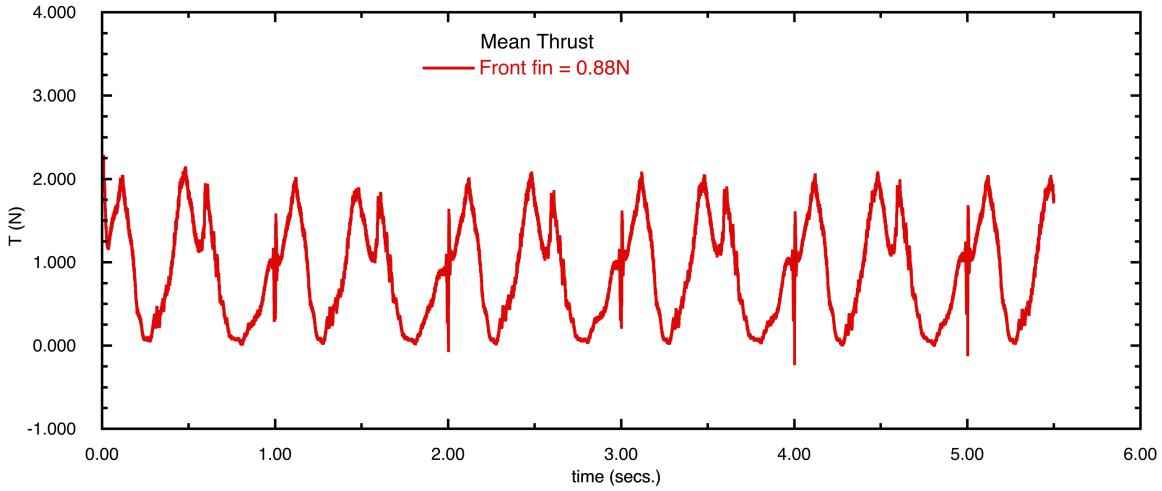


Fig. 8. Thrust time history for a flexible fin flapping at 1Hz.

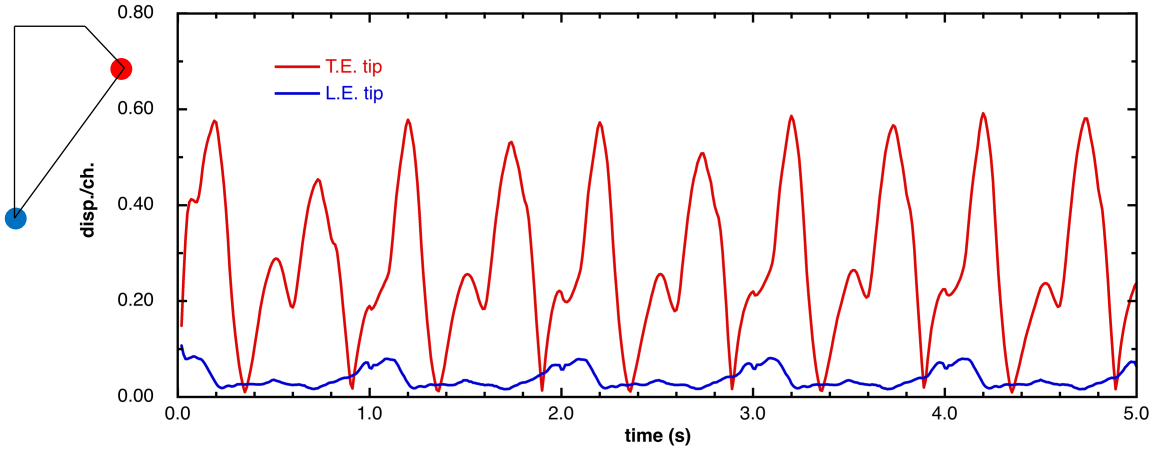


Fig. 9. Displacement of the leading and trailing edge tips of the flexible flapping fin.

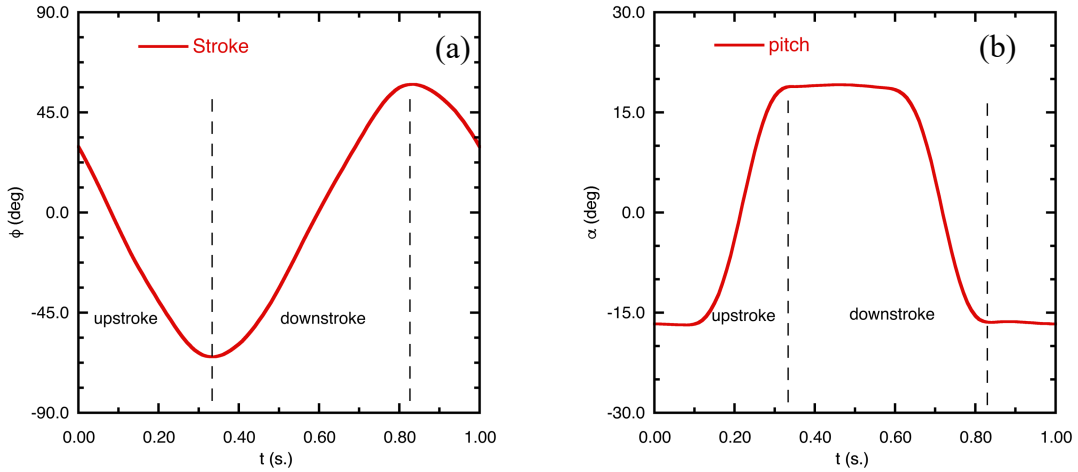


Fig. 10. Kinematics of tandem flapping fins(a) stroke angle and (b) pitch angle, $f$=1Hz, $\alpha_0$= 15°.

Reynolds number for the flow was based on the mean tip velocity, $V_{tip}$, and the chord, $C$, of the fin as

$$Re = \frac{\rho V_{tip} C}{\mu},$$
$$V_{tip} = 2\Phi R f. \qquad (18a,b)$$

Here, $R$ is the distance between the tip of the leading edge of the fin from the center of stroke rotation, $f$ is the flapping frequency, and $\Phi$ is twice the stroke amplitude. The Reynolds number for this flow with an average $C$=5cm and $R$ = 18.175cm, is 38850.

The phase offset between the front and the rear fins are varied between ±180°, and the mean thrust from the fins are shown in Fig. 11. The rigid fins produce nearly 0.7N of thrust with the rear fin producing a maximum thrust of 0.77N when it is lagged by 90°. The front fin of the flexible pair produces nearly 0.94N of thrust with the rear fin producing maximum thrust of 1.3N and 1.21N, at 2 phase offsets, δ = -135° and +45°, respectively. The thrust time history of the rigid, flexible fin at the baseline offset is shown in Fig. 12. For the flexible fin, both the front and rear fins gain some thrust at the beginning of the upstroke, t = 0.8-0.9s, and the rear fin produces more thrust in the middle of the downstroke, t = 0.55-0.75s, highlighted in Fig. 12b. The time history of the thrust for the flexible fin at the peak thrust offsets of δ = -135° and +45°are shown in Fig. 13. In these cases, the rear fin attains a peak thrust in the middle of the upstroke, between t = 0.4-0.6s, and in the middle of the downstroke, t = 0.9-1.1s, for δ = -135°, shown in Fig. 13a, and vice-versa for δ = 45°, in Fig. 13b. The surface pressure on a spanwise plane cut through the trailing edge tip for the rigid and the flexible fin at the an instant when the thrust is maximum for δ = -135° is shown in Figs. 14a and b. For the flexible fin, the high pressure on the top surface acts on a larger projected area in the thrust direction, leading to a much higher thrust. In addition to this, in the flexible case, the induced velocity at the leading edge of the trailing fin is increased by the shed vortex for the trailing edge of the front fin, shown in Fig. 15. The vortex shed from the trailing edge is seen in the spanwise vorticity at t= 4.25s in Fig. 16b. Similar effect is seen on the middle of the downstroke, but several pairs of trailing edge vortices of lesser strength are shed from the front fin during its previous stroke, Fig. 16a, leading to a lesser peak in thrust of 2N compared to the upstroke peak of 3N, seen in Fig. 13a. The trailing edge vortices shed around 0.25s, assuming

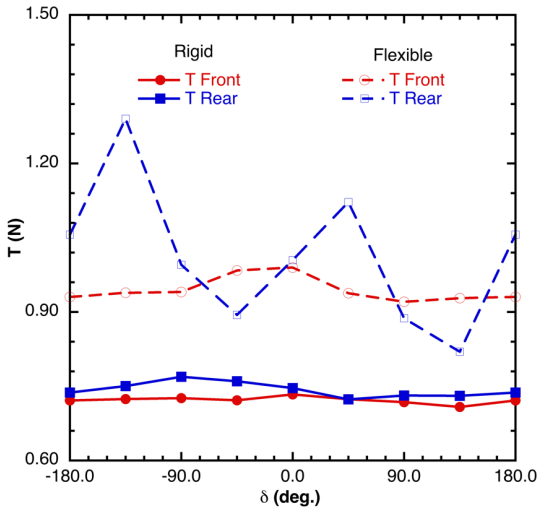


Fig. 11. Thrust production from flapping fins for various pitch offsets, $x_{offset}$= 15cm, $f$ = 1Hz.

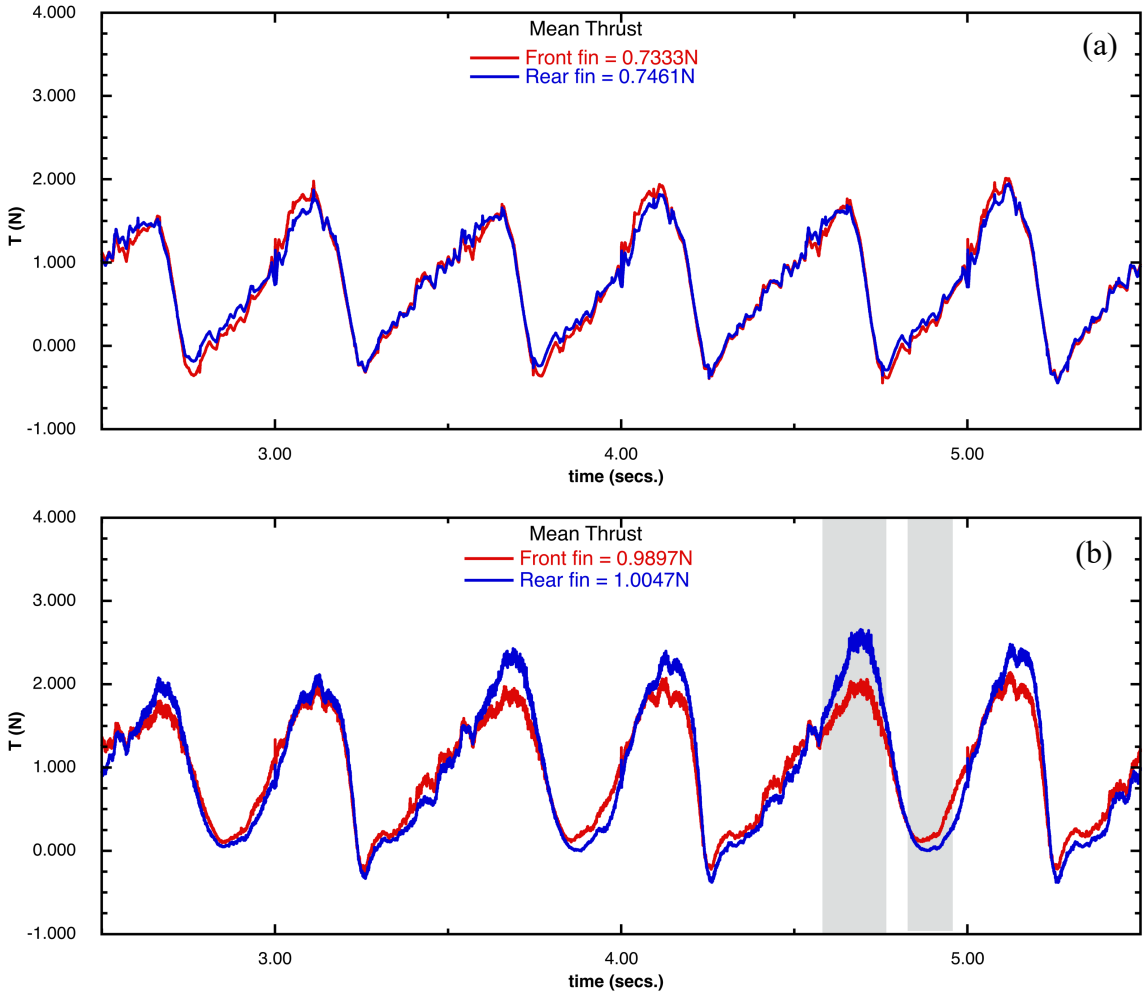


Fig. 12.Time history of thrust for tandem flapping (a) rigid fins and (b) flexible fins, $\delta = 0°$.

are advected at the mean tip velocity of 0.77m/s would reach the leading edge of the rear fin in approximately 0.2s, giving rise to the increased thrust production during the middle of the upstroke. Figure 17 shows the excursions of the leading and trailing edge tips for the case with a phase offset $\delta = -135°$, and the trailing edge tips reach a peak value of close to 1.5*C*.

The rear flexible fin produces two local minima corresponding to offsets of -45° and 135°, see Fig. 11. At a phase offset of $\delta = -45°$, Fig. 18a, the rear fin loses thrust throughout the stroke, although it achieves a higher thrust peak in the middle of the upstroke, which is offset by the narrower thrust production during the upstroke and the increased drag produced at the end of the upstroke. Similar reduction is seen at the phase offset of 135°, Fig. 18b, throughout the stroke.

In addition to the flexible fin with E = 0.75MPa, another more flexible material with 0.31MPa was simulated. The mean thrust production is similar to the 0.75MPa material. Again, the rear fin in this case attains two peaks at $\delta = -135°$ and +45°. This more flexible material will be used in further studies with a closer spacing between the two fins.

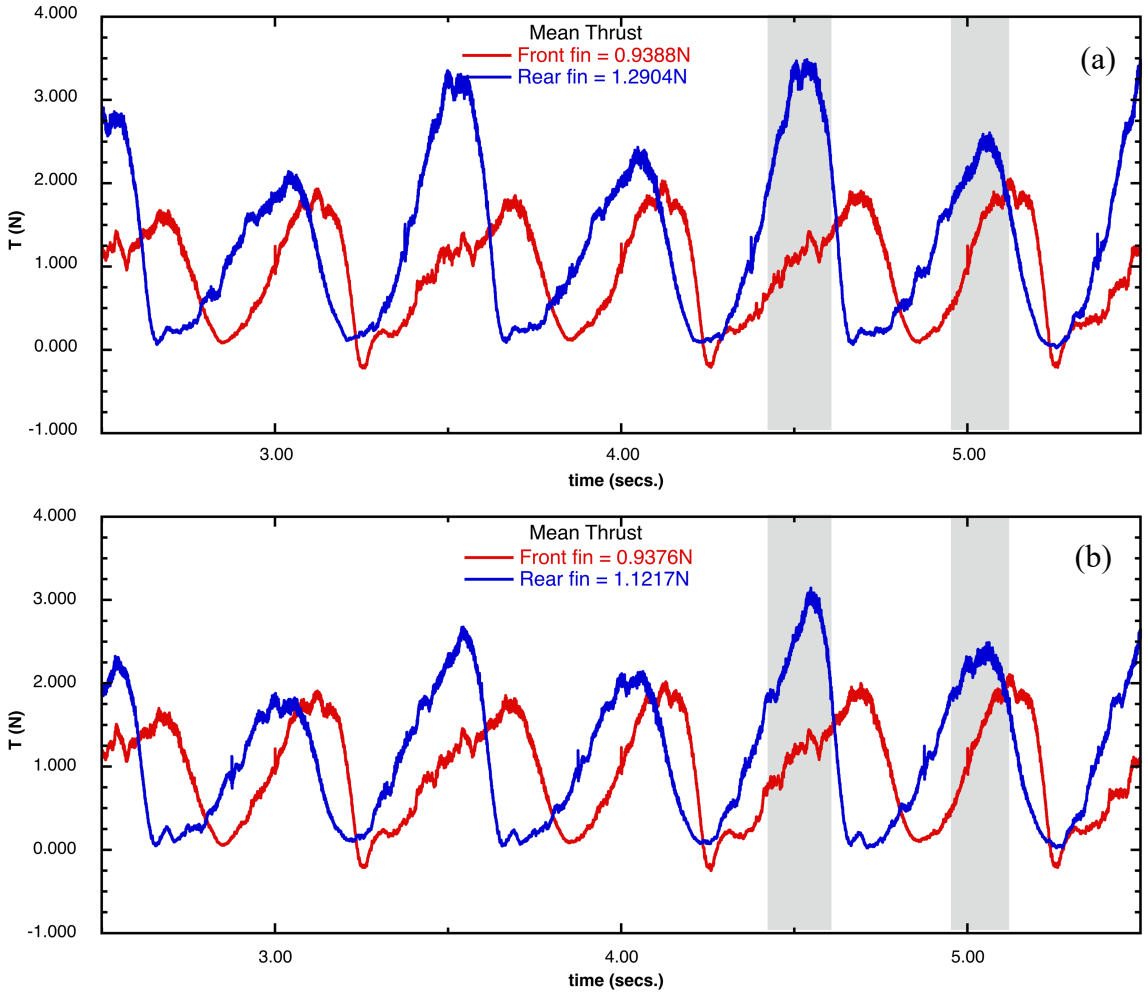


Fig. 13.Time history of thrust for tandem flapping flexibles fins (a) δ = -135°, and (b) δ = 45°.

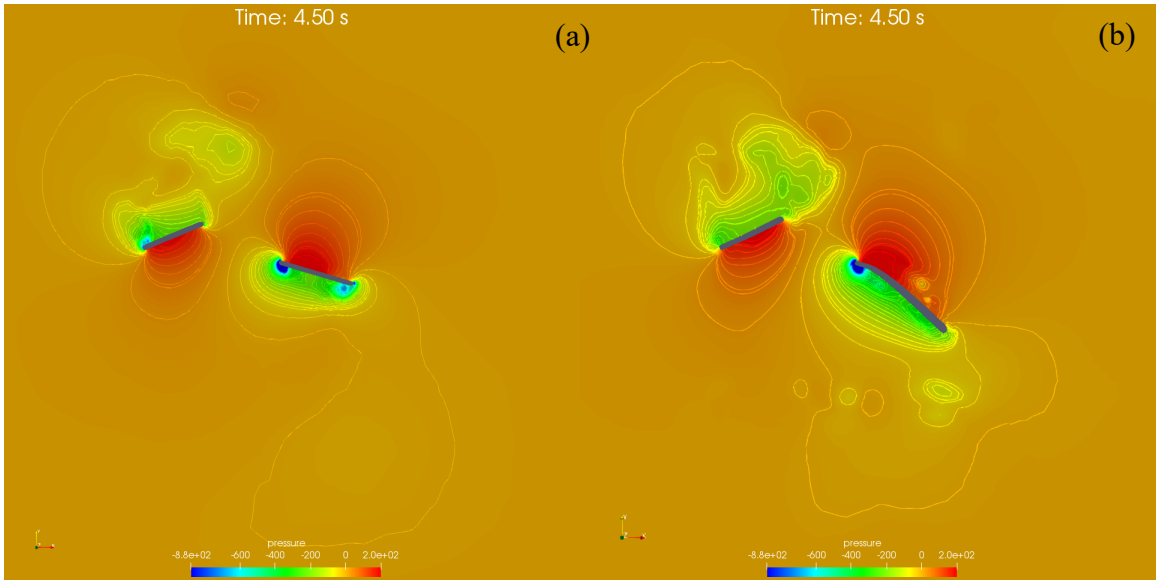


Fig. 14. Instantaneous pressure distribution in the middle of the upstroke, t= 4.5s on the fin on a plane *z*= 3.0, δ = -135°, (a) rigid fin, and (b) flexible fin.

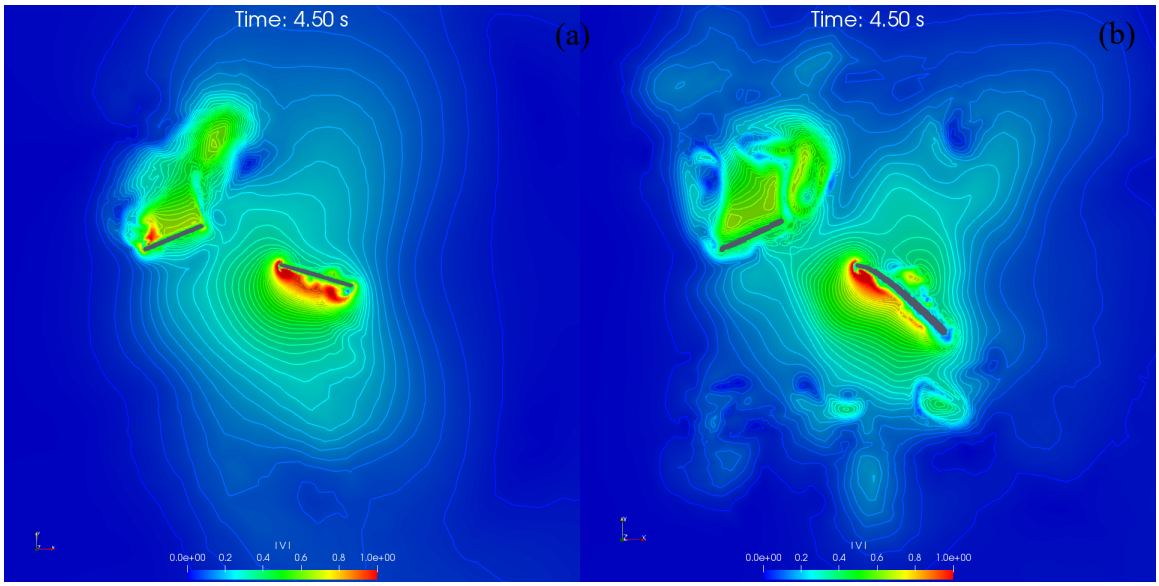


Fig. 15. Instantaneous magnitude of velocity in the middle of the upstroke, t= 4.5s on the fin on a plane *z*= 3.0, δ = -135°, (a) rigid fin, and (b) flexible fin.

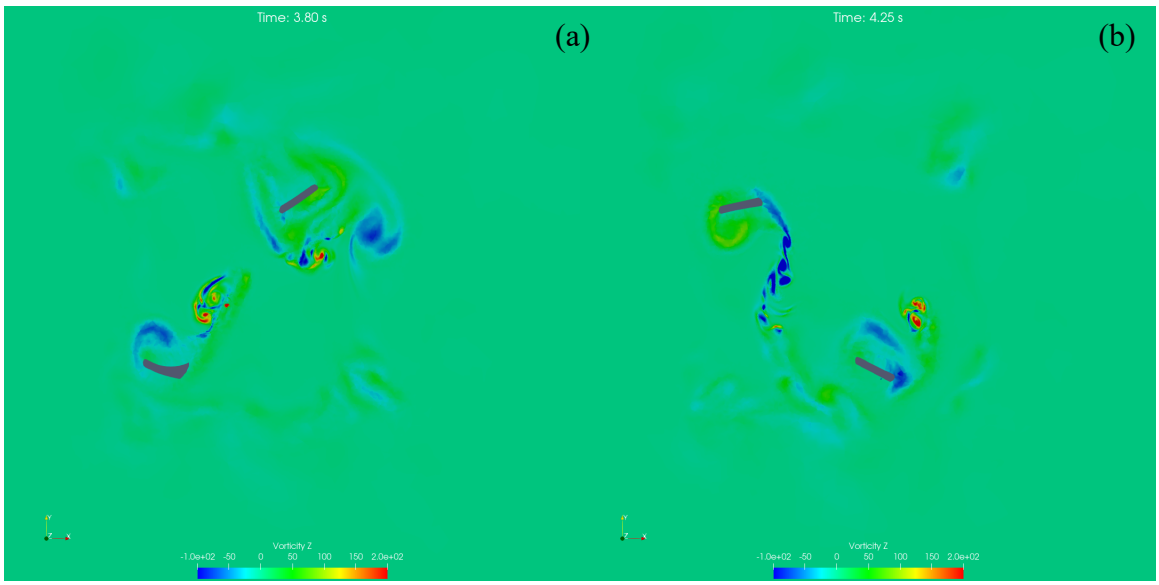


Fig. 16. Spanwise vorticity on a plane *z*= 3.0, for the flexible fin showing the trailing edge vortices shed during (a) downstroke at t = 3.8s and (b) the upstroke at t=4.25s, δ = -135°.

*Pitch amplitude 45°:*

Another set of kinematics with a much higher pitch amplitude, $\alpha_0$= 45°, shown in Fig. 19, was used. The stroke amplitude is similar to the previous kinematics of 61°. Figure 20 shows the mean thrust from the fins at various phase offsets. Here, the rigid front fin produces nearly 1.2N of thrust and the flexible front fin produces 1.1N. The rear fin in the rigid pair produces more than 1.3N with a maximum of 1.54N occurring at a phase lag of 90°. Similar trend is observed with the flexible fin but with a reduced mean thrust by nearly 0.1N. Figure 21 shows the comparison of

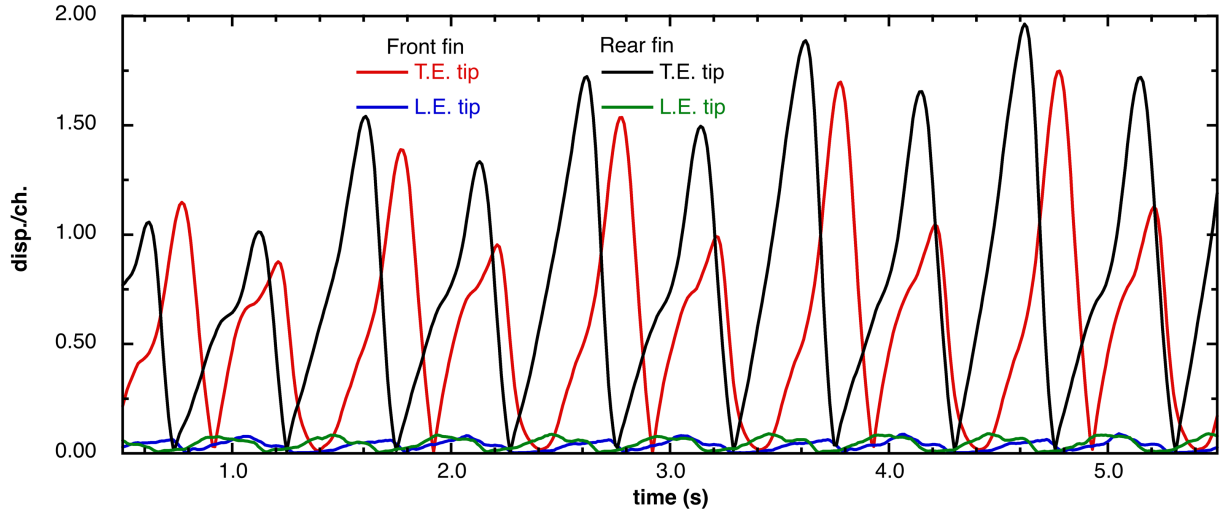


Fig. 17. Displacement of the leading and trailing edge tips of the flexible flapping fin, δ = -135°.

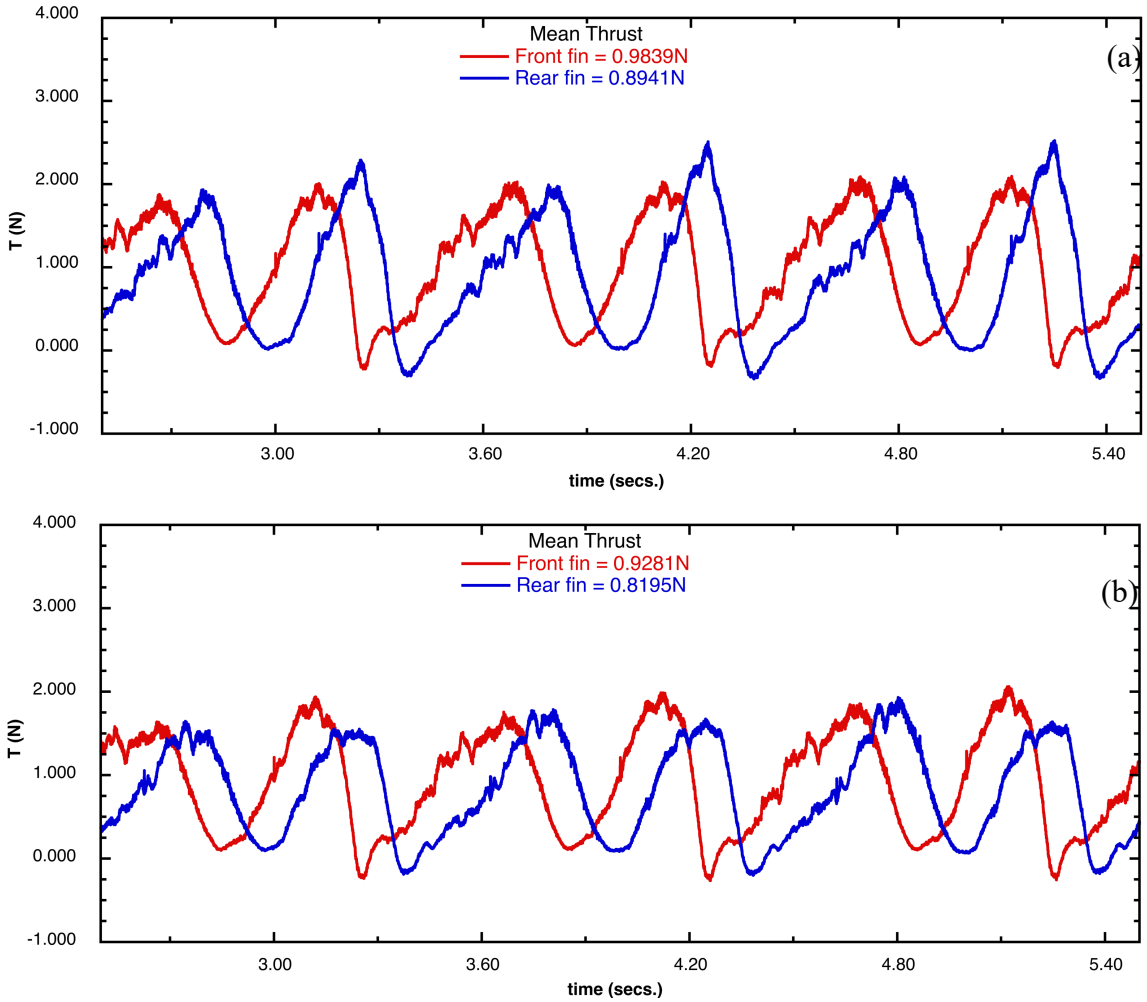


Fig. 18. Time history of thrust for tandem flapping flexibles fins (a) δ = -45°, and (b) δ = 135°.

time history of thrust production between the rigid and flexible fins at the peak phase offset of δ = -90°. The front fins in both cases produce nearly the same men thrust of 1.1N, except for the upstroke for the rigid fin producing a small extra thrust. The rigid rear fin, on the other hand, exhibits the same thrust production during the upstroke, t = 0.1-0.5s, and an enhanced thrust production during the downstroke, t = 0.6-1.1s, leading to a higher mean thrust of 1.54N compared to the flexible fin's 1.41N. In the middle of the stroke, much higher pressure exists on the lower side of the rigid fin, Fig. 22a, compared to the flexible fin, Fig. 22b, leading to the higher thrust in during that period. Also, the extent of the high pressure region is more on the front fin for the rigid case compared to the flexible case, again leading to the small extra thrust from it. The trailing edge vortex shed from the front fin surrounds the leading edge of the rear fin, Fig. 23a, compared to the flexible fin, Fig. 23b, where it is entirely above it, leading to a much stronger leading edge vortex on the rear fin. The displacement of the leading and trailing edge tips for the δ = -90° case is shown in Fig. 24, and the peak excursion is nearly half of the previous kinematics.

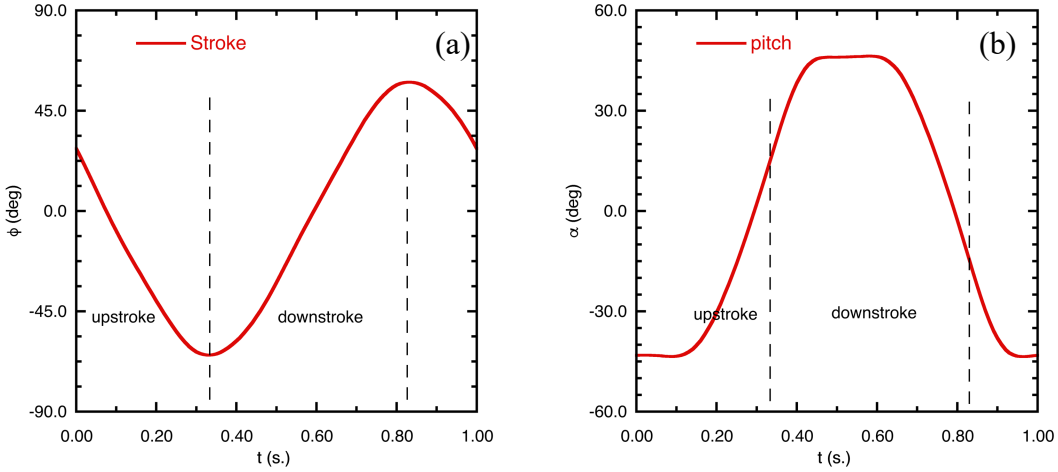


Fig. 19. Kinematics of tandem flapping fins(a) stroke angle and (b) pitch angle, $f$=1Hz, $\alpha_0$= 45°.

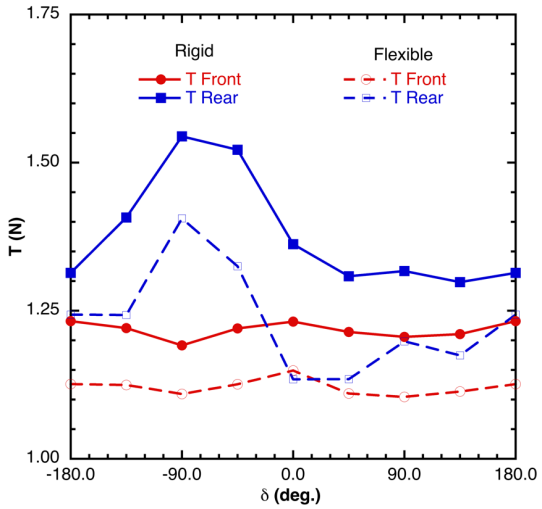


Fig. 20. Thrust production from flapping fins for various pitch offsets, $x_{offset}$= 15cm, $f$ = 1Hz.

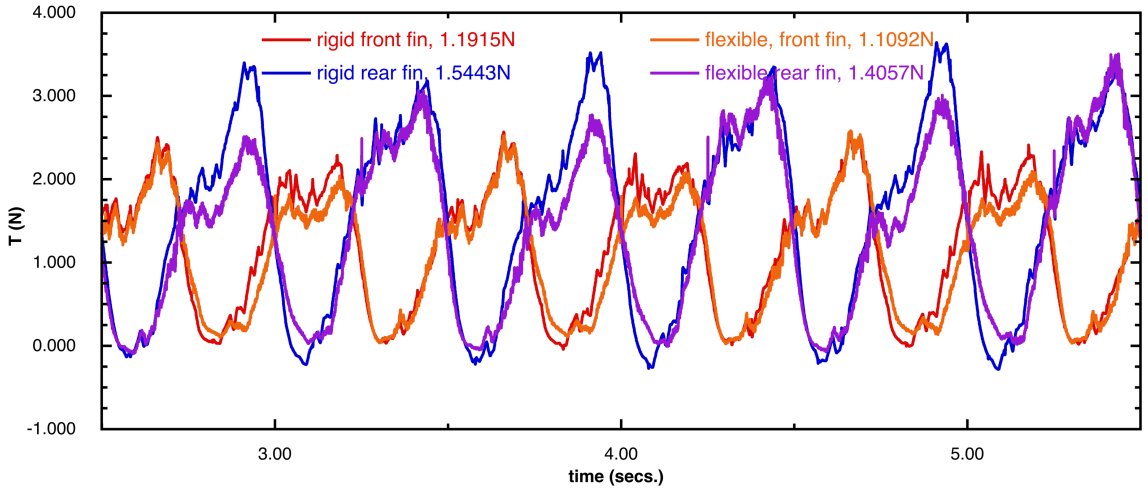


Fig. 21. Comparison of time history of thrust at between rigid and flexible fins, δ = -90°.

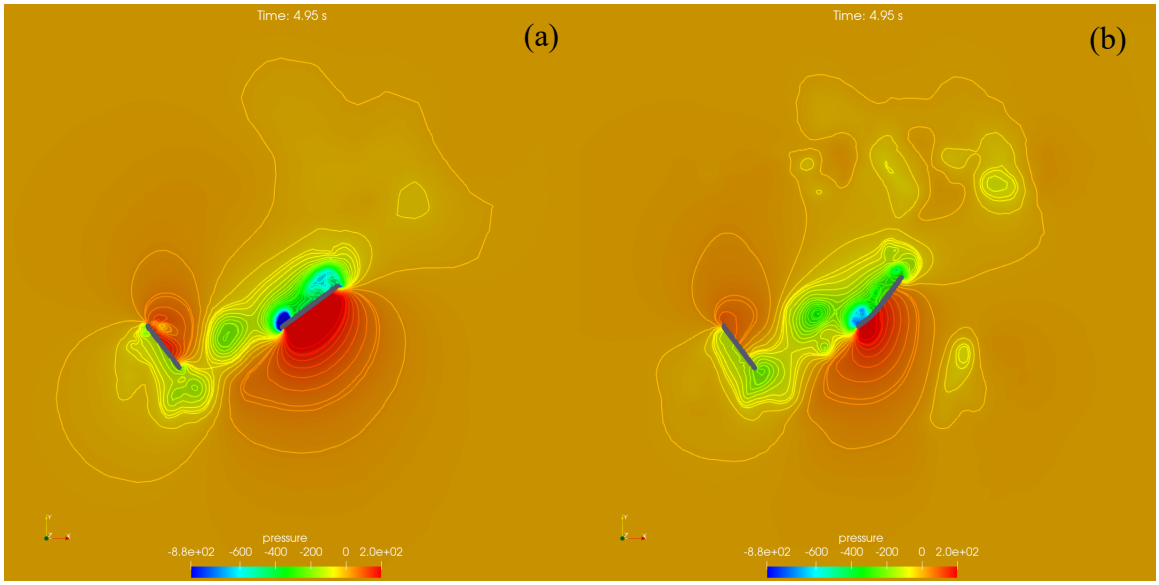


Fig. 22. Instantaneous pressure distribution in the middle of the stroke, t= 4.95s on the fin on a plane *z*= 3.0, δ = -90°, (a) rigid fin, and (b) flexible fin.

***Tandem Flapping fins separated by 12cm:***

Next, the coupled approach is applied to the another set of tandem flapping fins separated by 12cm. For this, a new set of fins were fabricated. The fins were tested for tensile stress, and the Young's moduli were determined to be 0.85MPa and 0.31MPa. The displacement for the modes for the two flexible fins is shown in Figs. 25 and 26. For the more flexible fin, E= 0.31MPa, first 15 modes were used in the simulation. The kinematics used for these simulations are at 2Hz with a pitch amplitude, $\alpha_0$= 15°, and is shown in Fig. 27. The rear fin in this case lags the front fin in pitch rotation and is shown in Fig. 27b.

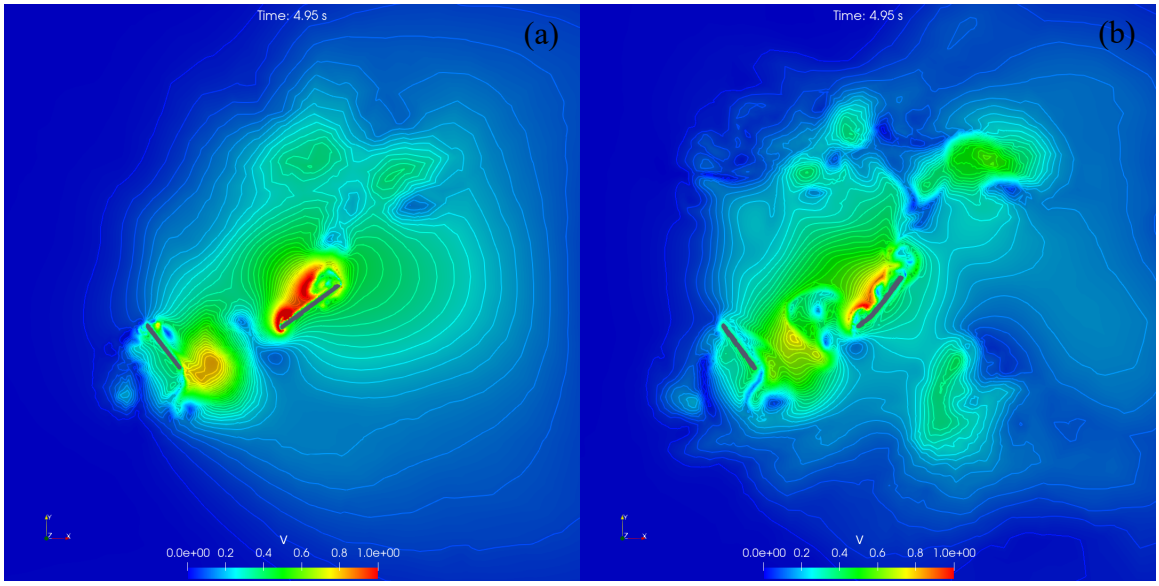


Fig. 23. Instantaneous magnitude of velocity in the middle of the stroke, t= 4.95s on the fin on a plane *z*= 3.0, δ = -90°, (a) rigid fin, and (b) flexible fin.

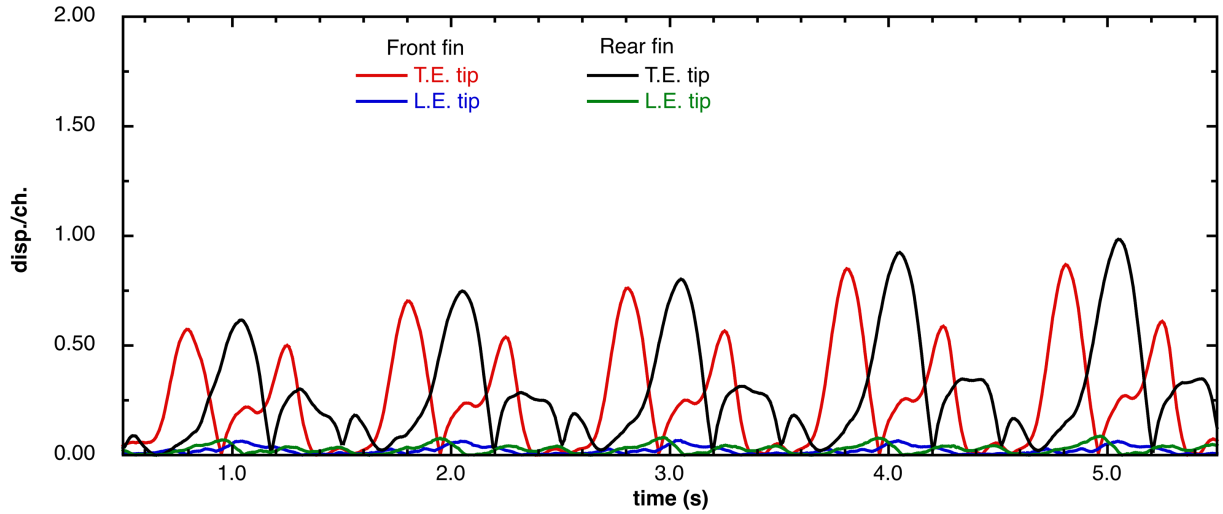


Fig. 24. Displacement of the leading and trailing edge tips of the flexible flapping fin, δ = -135°.

*Effect of flexibility:*

The mean force produced by the two fins for the rigid and the two flexible fins are shown in Fig. 28. The rigid front fin produces nearly 0.7N for all phase offsets, and the rear fin achieves a maximum peak of 0.74N when lagged by 67.5° and a minimum of 0.64N when leading the front fin by 67.5°, shown in Fig. 28a. For the flexible fin set with E = 0.85MPa, the front fin produces 0.89N with a small peak at δ = 0° of 0.92N, while the rear fin produces less thrust compared to the front fin. The maximum peak thrust for the rear fin occurs when it is lagged by 135° and a minimum occurs when it leads by 45°. For the more flexible fin with E = 0.31MPa, both the fins produce less thrust compared to the rigid fins. The front fin in this set produces nearly 0.64N of thrust, while the rear fin attains a maximum value of 0.59N at δ = -135°, and a minimum of 0.49N when it leads the front fin by 90°. This trend is quite different in that the rear fin produces less

thrust compared to the front fin and the reasons for this behavior will be explored next. Figures 28b and c show the lift and the side forces produced. It is clear that the front fins produce negligible lift force, Fig. 28b, except near the peak offsets of the thrust production for the flexible fins. The front fins on the other hand, Fig. 28c, produces a small side force directed towards the rotation axis, while the rear flexible fins exhibit a small variation with respect to the phase offsets.

Figure 29 shows the time history of thrust production at $\delta = -135°$, for the three fins. The rigid rear fin produces nearly 0.72N compared to the front fin's thrust of 0.69N. Most of the increased thrust from the rear fin is during its upstroke, t = 4.17-4.42s, with the peak thrust occurring near t= 4.34s. At this instant, the rear fin is subjected to an increased induced velocity form the trailing edge vortex shed from the front fin around t = 4.25s. Similar trailing edge vortex is shed from the front fin at t = 4.48s, but it lies far below the leading edge of the rear fin during its downstroke. This is evident from the instantaneous pressure, velocity and spanwise vorticity during the middle of the upstroke of the rear fin, shown in Fig. 30.

The effect of flexibility on the front fin thrust is also seen from the Fig. 29. The flexible fin with E = 0.85MPa, produces 0.87N compared to 0.69N for the rigid fin. This flexible fin produces extra thrust during the second half of both the up and downstrokes, t= 4.10-t=4.25s and t= 4.38-4.50s, respectively, whereas the more flexible fin with E= 0.31MPa, produces less thrust during the entire upstroke and during the first half of the downstroke, leading to a reduced mean thrust of 0.63N. This is due to both reduction in the projected area of the more flexible fin during this part of the stroke compared to the other two fin for some part of the stroke, shown in Fig**.** 31, and more so with the reduced surface pressure on the top surface of the fin. The instantaneous pressure near the middle of the upstroke of the front fin is shown in Figs. 32 and 33. It is clear from the pressure on the plane cut that although the flexible fin, Fig. 32c, has more surface area in the thrust direction compared to the rigid fin, and nearly the same area as the flex fin with E= 0.85MPa, Fig. 33b, the thrust is reduced due to the reduced pressure on the top surface. Also, the pressure differential is reduced for the flexible fin with E= 0.31MPa compared to the other two, with the center of pressure situated near the tip of the fin.

Comparing the time history of the thrust produced by the rear fin for the two flexible fins, it is clear that the more flexible fin loses thrust in the downstroke between t= 4.5 and 4.6s. Figure 34 shows the pressure distribution on the plane cut through the trailing edge at the peak instant of t = 4.57s during the downstroke of the rear fin. Although, the cross section of the rear fin and the projected area at this instant are very similar, the pressure of the top surface of the more flexible fin is much reduced compared to the more rigid fin. This is partly due to the trailing edge vortex that is shed by the front fin around t= 4.32s, shown in Fig**.** 35 a and c, reaches the leading edge of the rear fin far below at t= 4.42s, Fig**.** 35 b and d, producing a lesser induced velocity. During the upstroke of the rear fin, t = 4.18-4.43s, both flexible fins exhibit nearly the same thrust production with the peak thrust occurring around t =4.32s, during the middle of the upstroke. Figure 36 shows the pressure distribution at this instant.

Figure 37 shows the trailing edge displacement of the two flexible fins with respect to the rigid fins position. During the upstroke, the front fin of the flexible fin with E= 0.85MPa reaches a peak displacement of nearly1*C* while the more flexible fin is nearly 1.45C. During the downstroke, the more flexible front fin reaches a peak displacement of nearly 2C. The rear fin reaches a peak value of 1.1C during the upstroke and 0.9C during the downstroke for the flexible fin with E =0.85MPa. The more flexible rear fin exhibits a much higher displacements of 2C during the upstroke. For the more flexible fin the trailing edge lags the rest of the fin during the up and downstrokes, leading to this larger excursion.

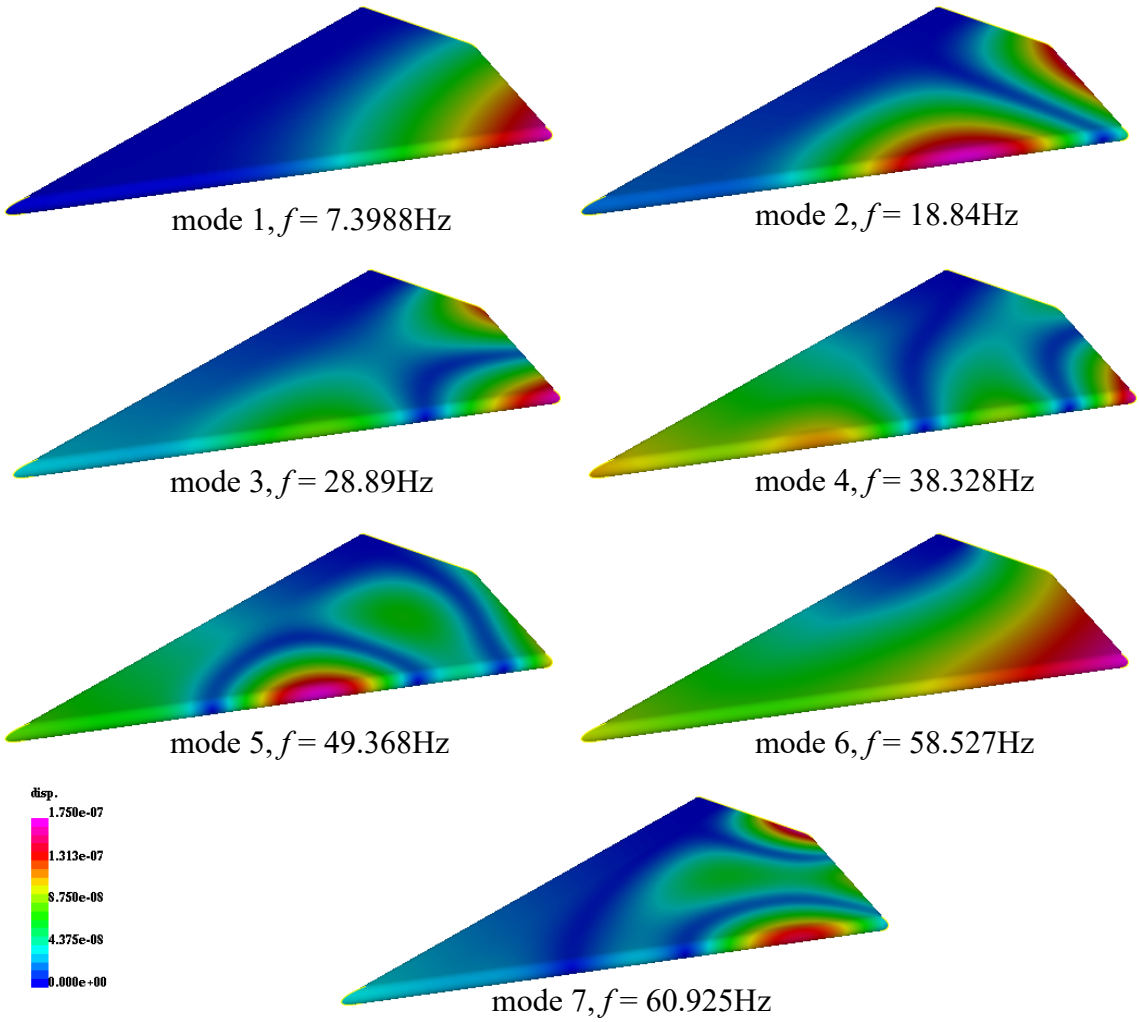


Fig. 25. Eigenmodes for the flexible fin, $E$ = 0.85MPa.

*Plane Cuts for PIV comparison:*

In the experiments, it was found that the both the rear flexible fins produced a maximum thrust when lagged by 112.5°, and a minimum thrust when it led the front fin by 67.5°. Also, in the experiments, the velocity at 3 plane cuts in the streamwise direction were monitored for these phase offsets. These planes include a midway plane between the trailing edge tip of the front fin and the leading edge of the rear fin, at $x$ = 10.5cm, a plane just downstream of the trailing edge of the rear fin, $x$ = 25.0cm and a plane far downstream at $x$ = 40.0cm. Detailed analysis of the evolution of velocity and the vorticity on these planes, its advection downstream and its effect on thrust production will be the main objective of a separate paper under preparation [13]. In this report, some of the time series of these plane cuts at these phase offsets at the maximum thrust production offset of 112.5° for all three fins are included for completeness. Figure 38 shows the

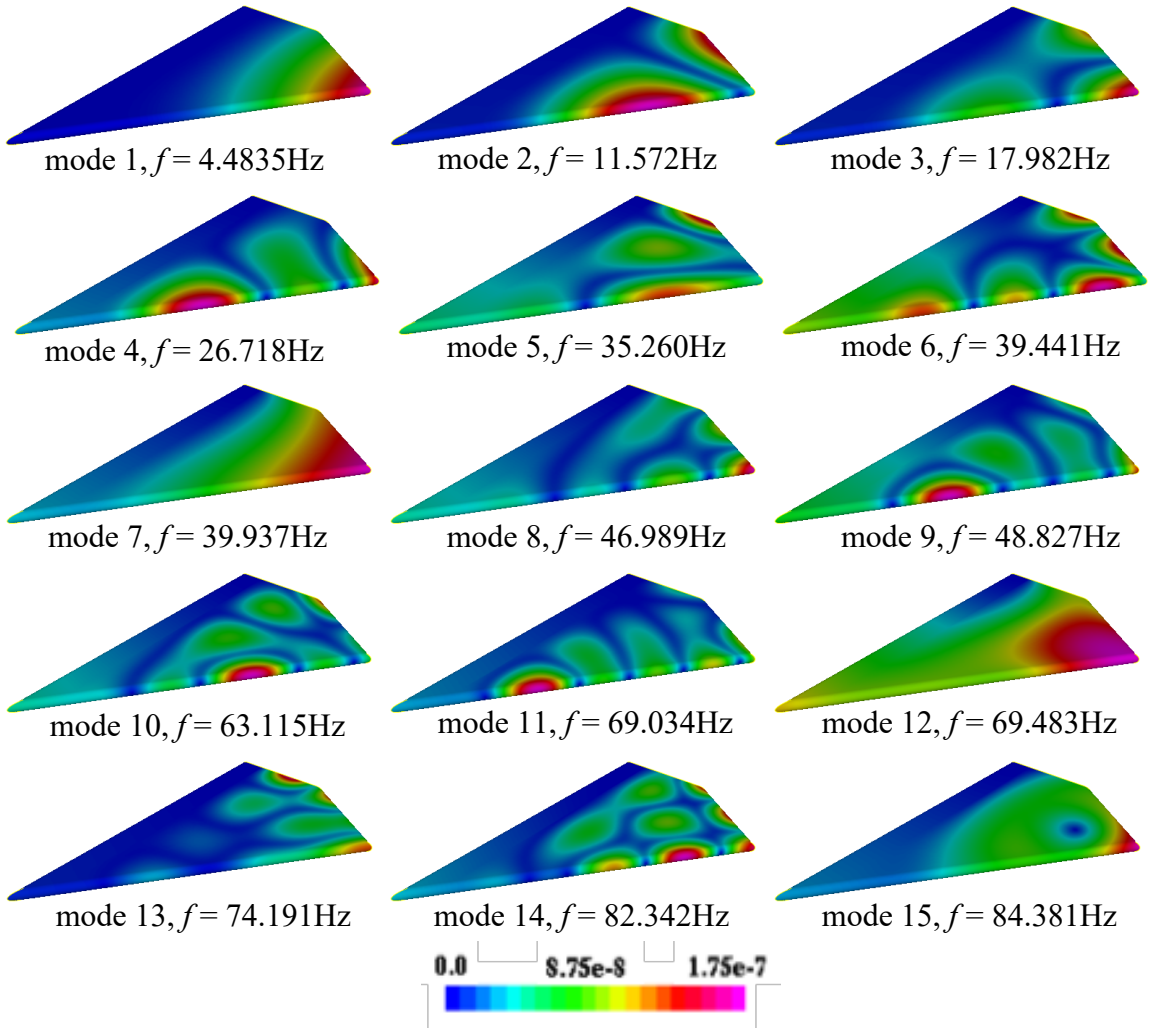


Fig. 26. Eigenmodes for the flexible fin, $E$ = 0.31MPa.

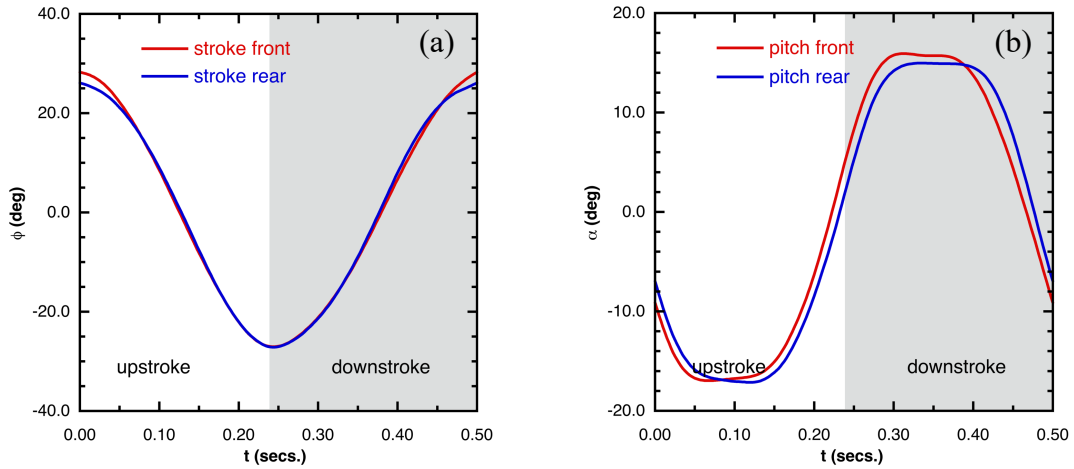


Fig. 27. Kinematics of tandem flapping fins (a) stroke angle and (b) pitch angle, $f$ =1Hz, $\alpha_0$= 15°.

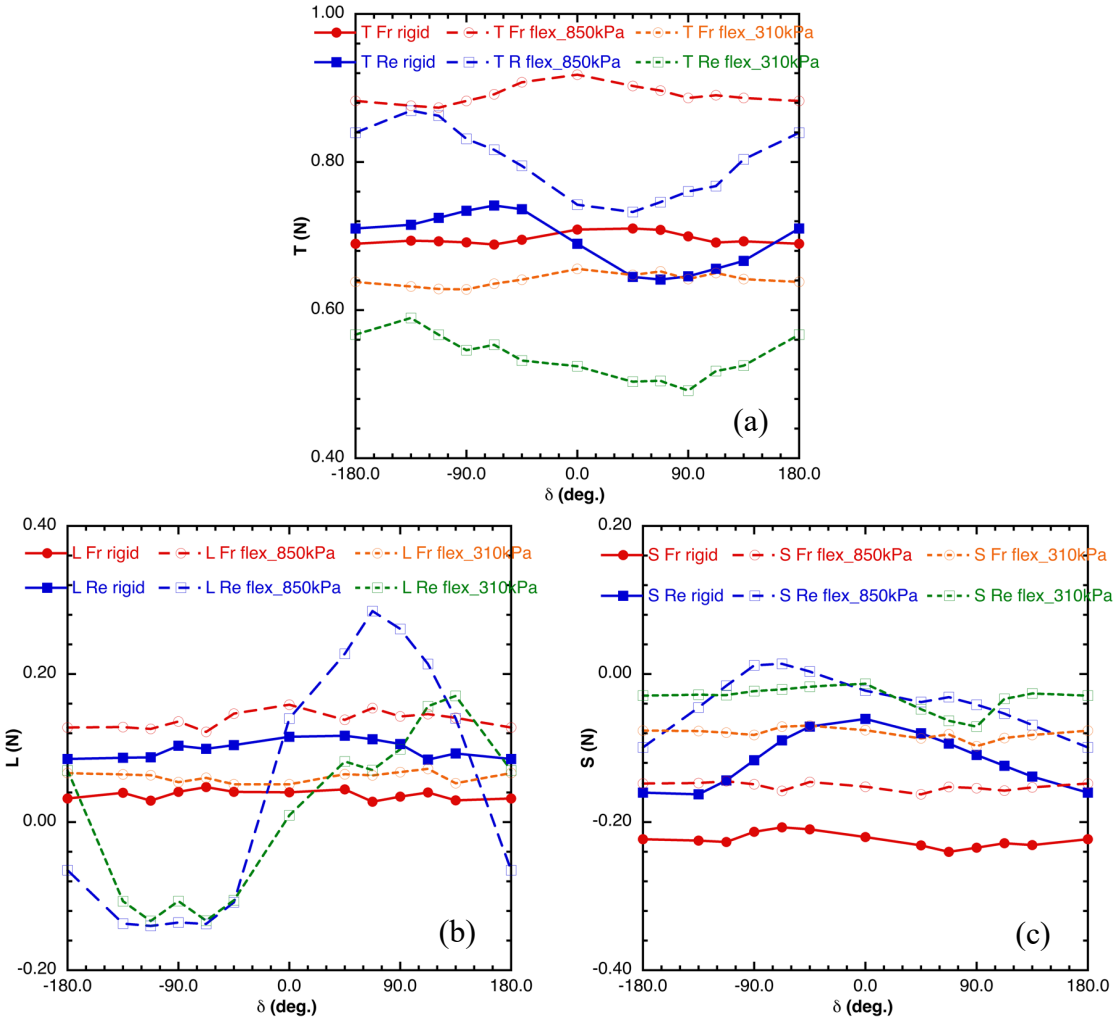


Fig. 28. Force production from flapping fins for various pitch offsets, (a) thrust, (b) lift and (c) side force $x_{offset}$= 12cm, $f$ = 2Hz.

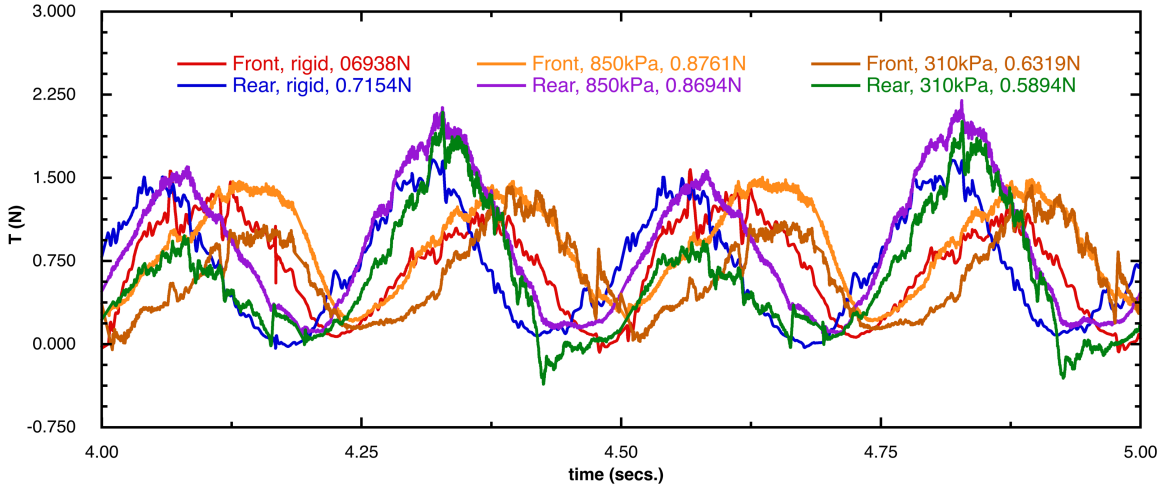


Fig. 29. Comparison of time history of thrust at between rigid and flexible fins, δ = -135°.

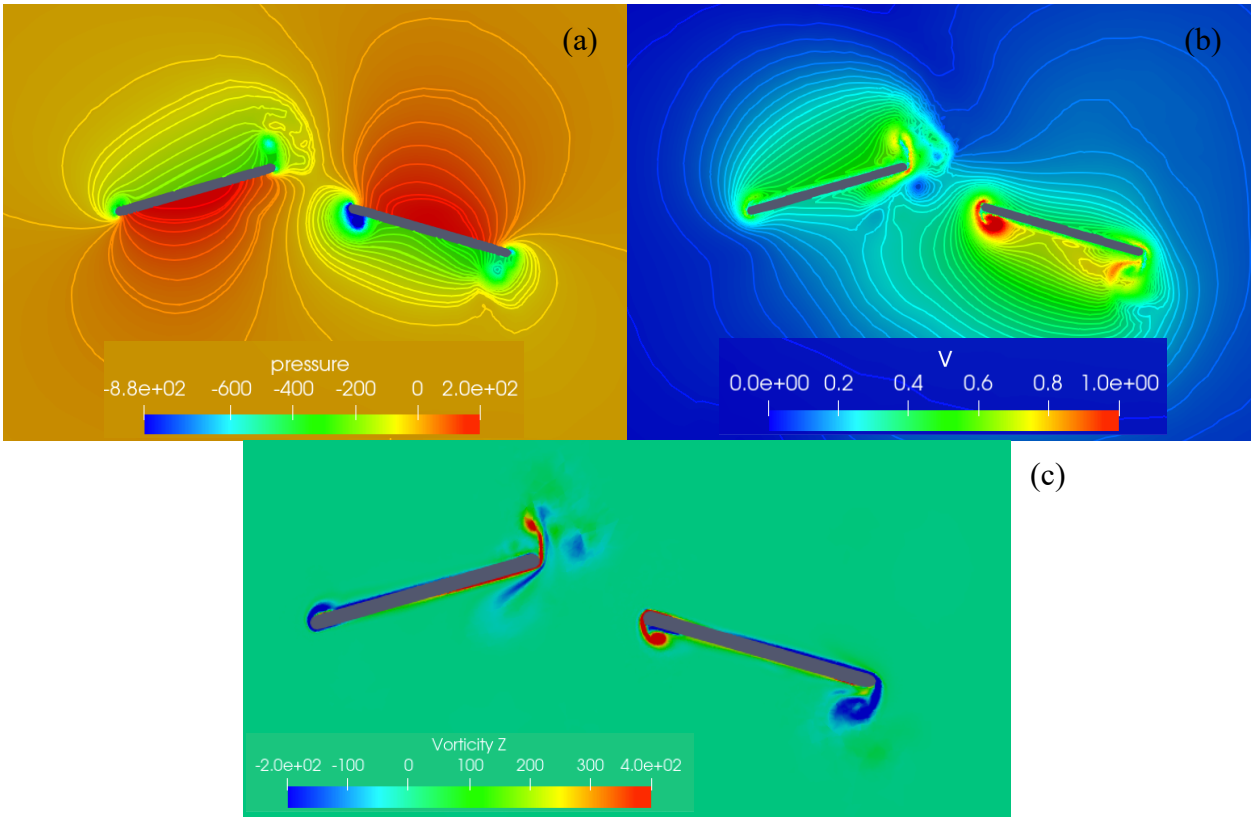


Fig. 30. Instantaneous distribution of (a) pressure, (b) magnitude of velocity and (c) spanwise vorticity on a plane z = 3.0, near the peak thrust production of the rear rigid fin, t = 4.34s, δ = -135°.

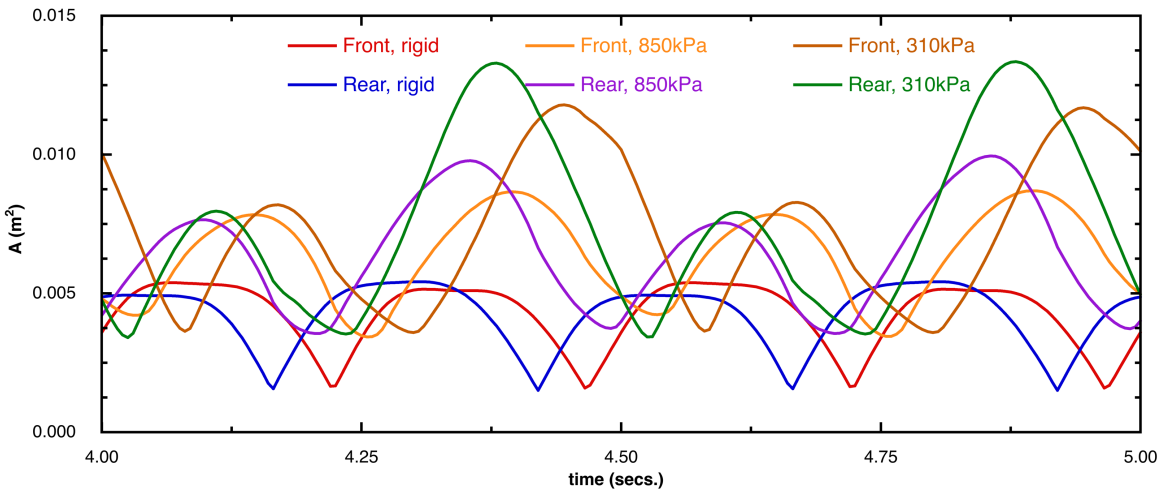


Fig. 31. Time history of projected area in the thrust direction.

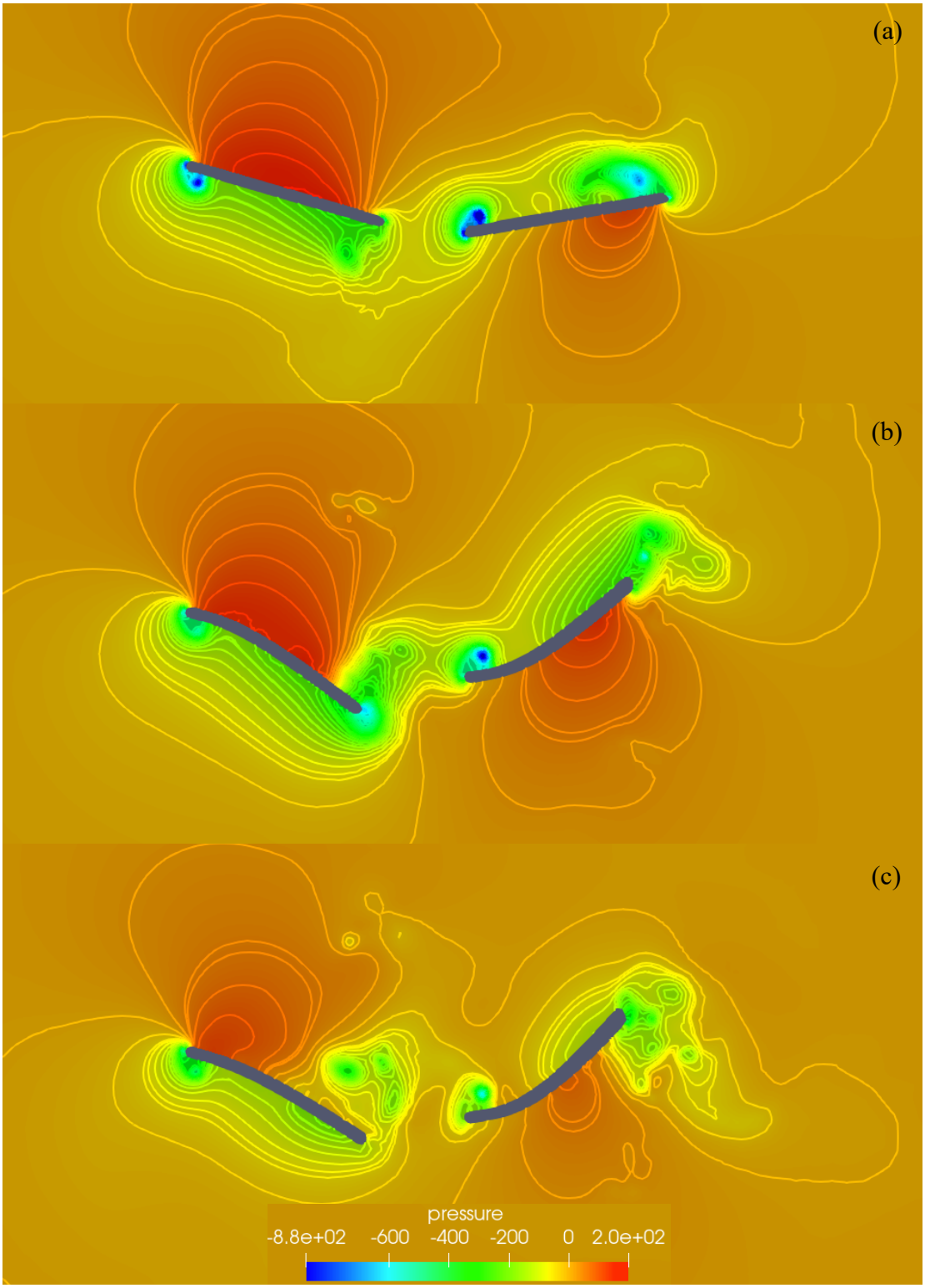


Fig. 32. Instantaneous distribution of pressure near the peak thrust production at t = 4.13s of the front fin, (a) rigid, (b) E= 0.85MPa and (c) E= 0.31MPa, on a plane z = 3.0, δ = -135°.

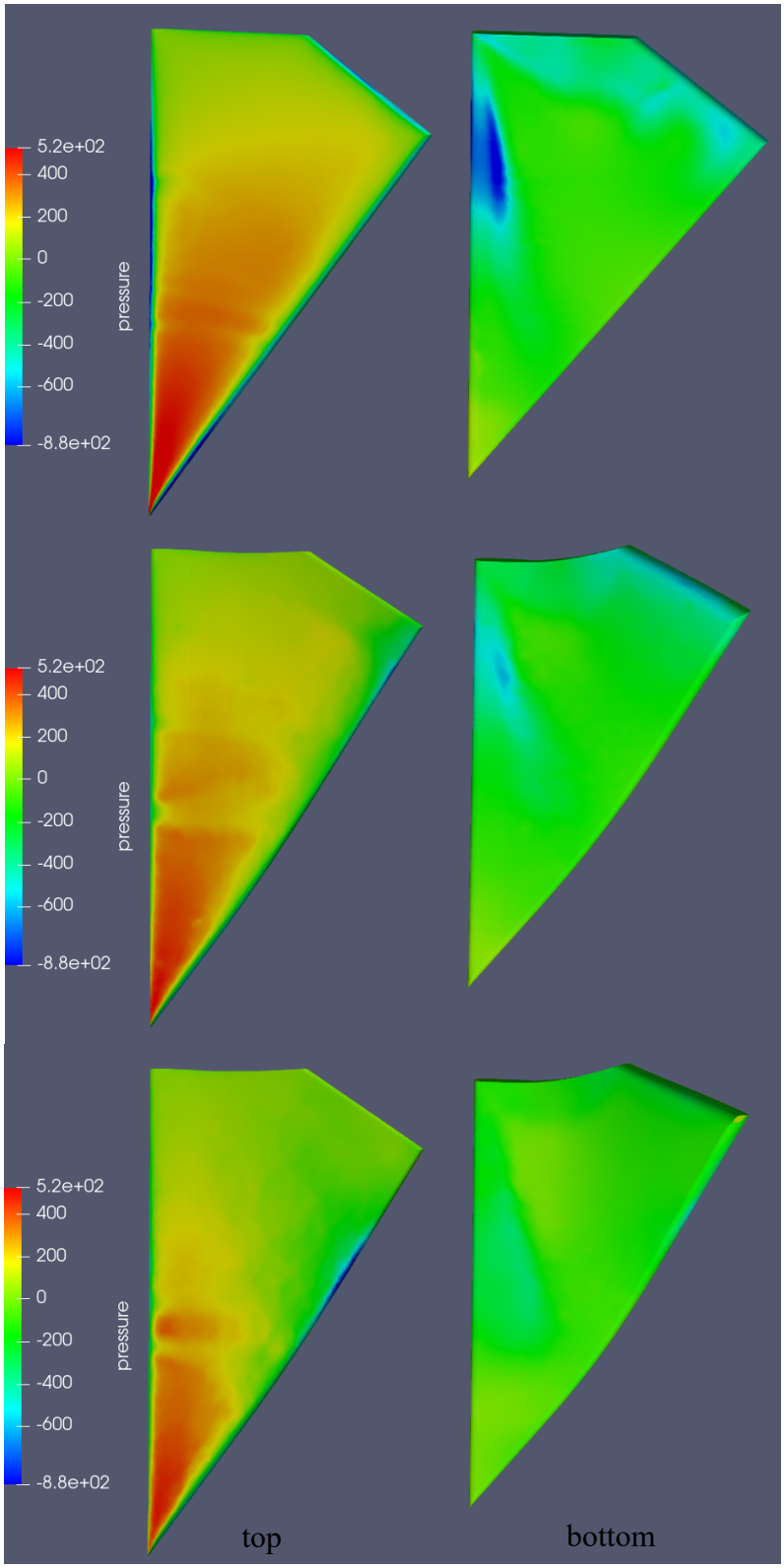


Fig. 33. Instantaneous distribution of pressure near the peak thrust production at t = 4.13s on the top (left) and bottom (right) surfaces of the front fin, (a) rigid, (b) E= 0.85MPa and (c) E= 0.31MPa, $\delta$ = -135°.

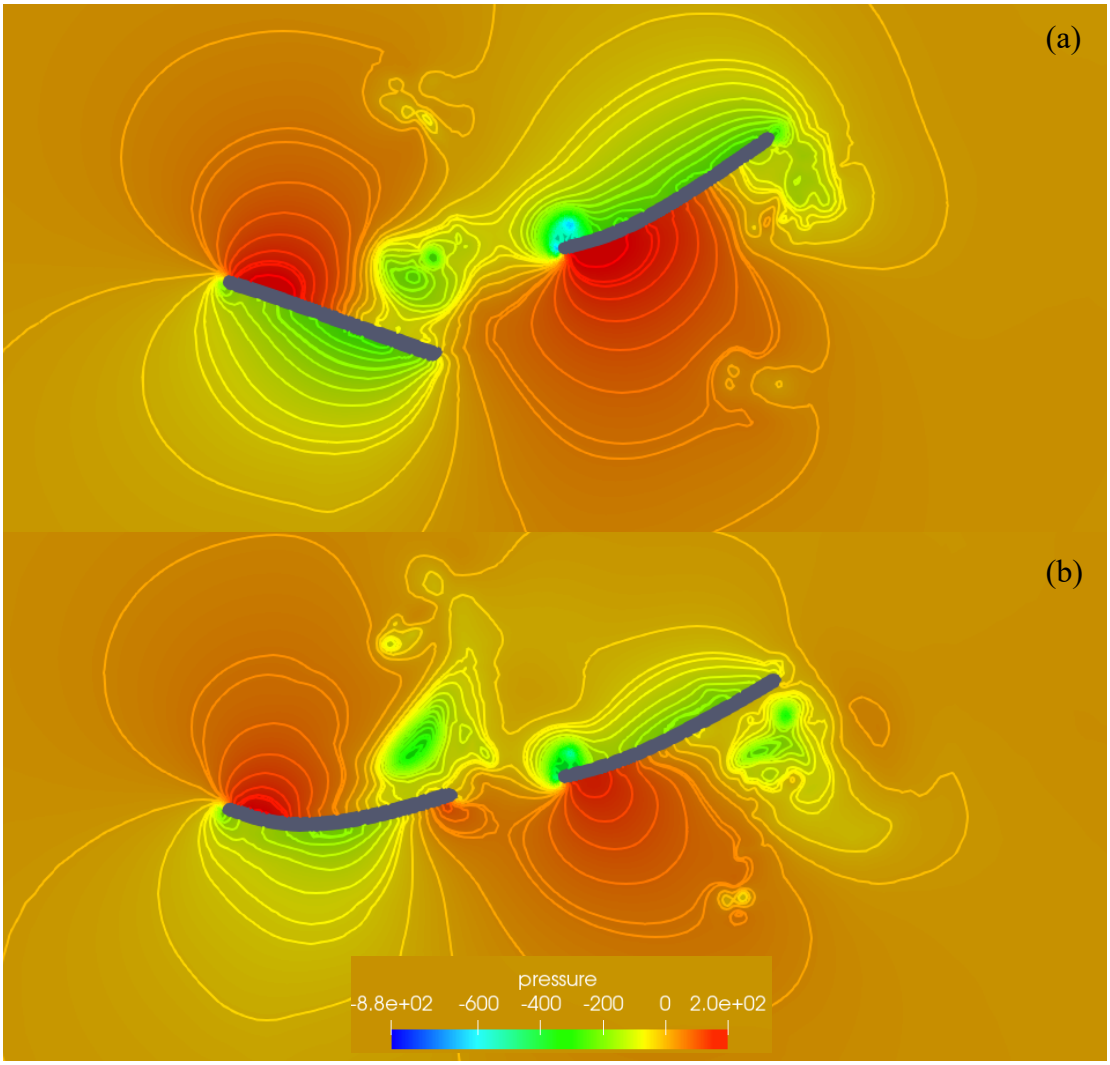


Fig. 34. Instantaneous distribution of pressure near the peak thrust production at t = 4.57s during the downstroke of the rear fin, (a) E= 0.85MPa and (b) E= 0.31MPa, δ = -135°.

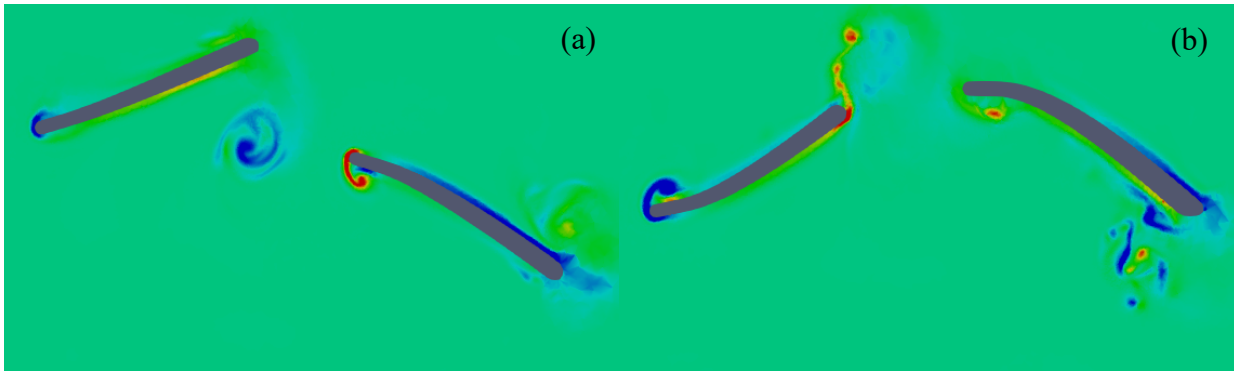

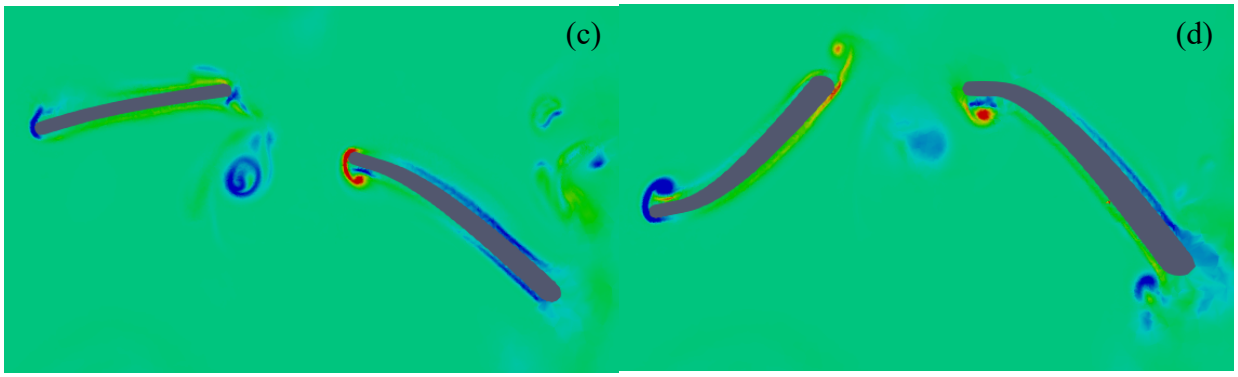


Fig. 35. Vortex interaction from the front fin shed (a,c) at t = 4.32s with the rear fin (b,d) at t= 4.42s, for the flexible fin (a,b) E= 0.85MPa and (c,d) E = 0.31MPa.

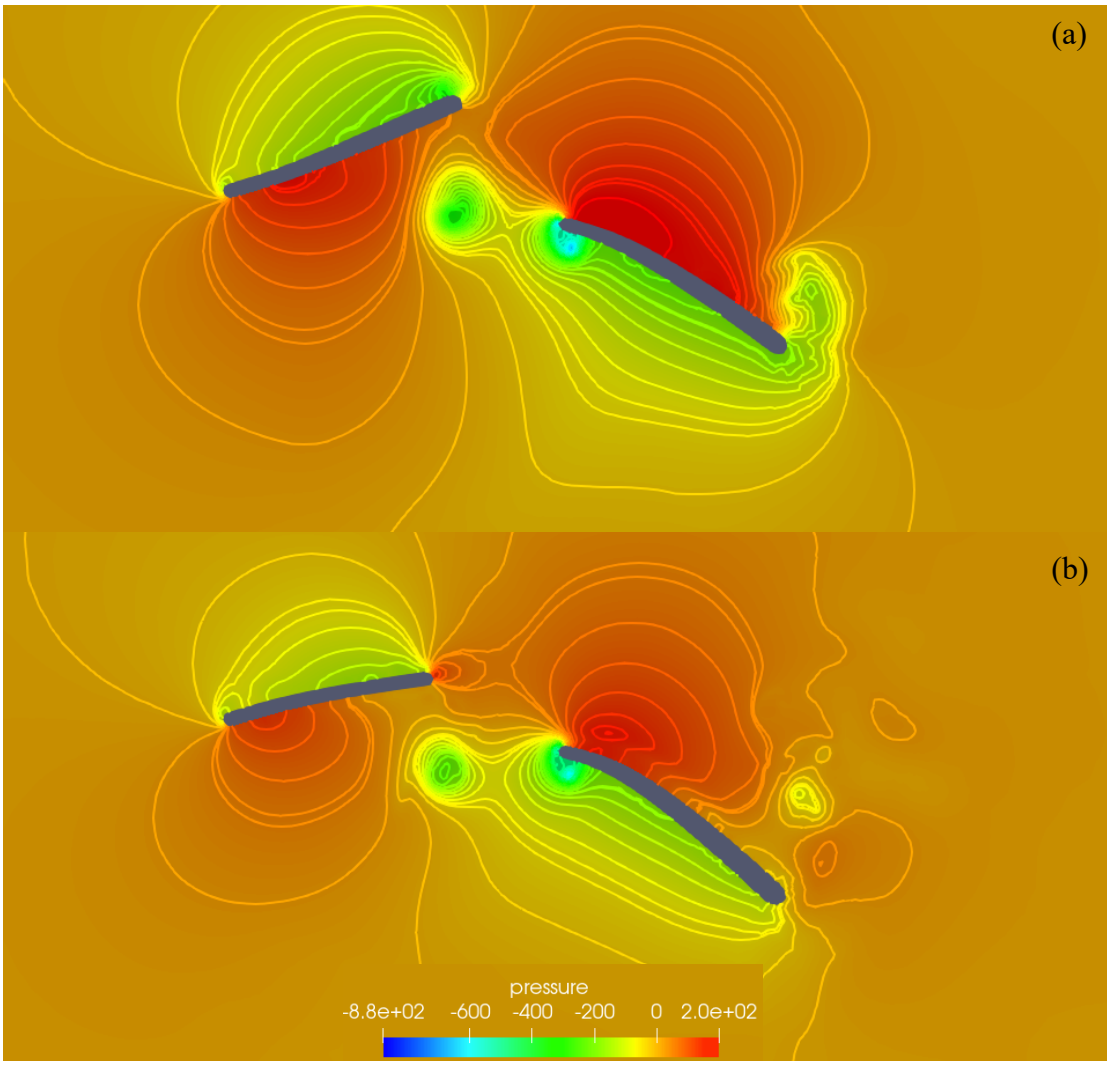


Fig. 36. Instantaneous distribution of pressure near the peak thrust production at t = 4.32s during the upstroke of the rear fin, (a) E= 0.85MPa and (b) E= 0.31MPa, $\delta = -135°$.

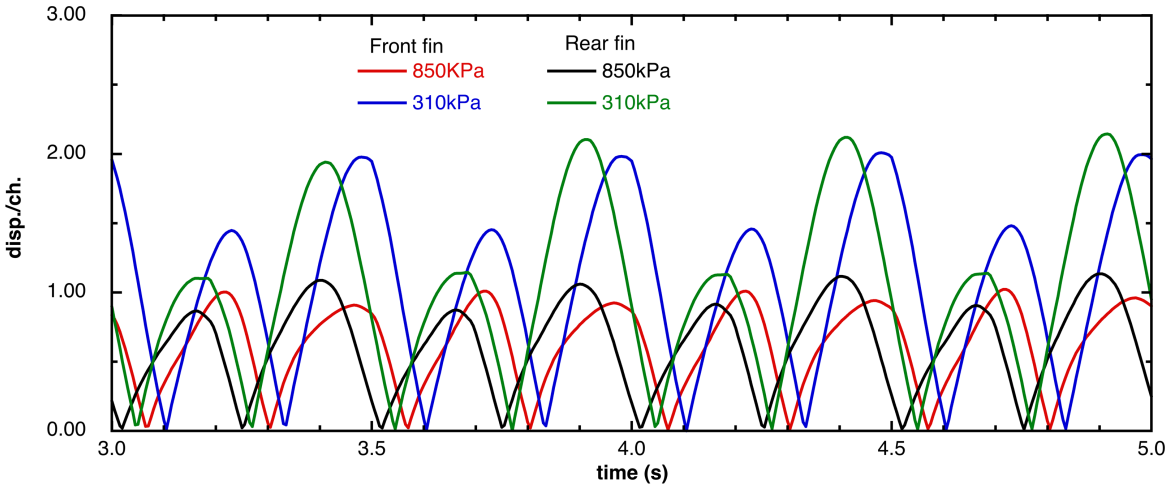


Fig. 37. Time history of the trailing edge displacement of the flexible fins, δ = -135°.

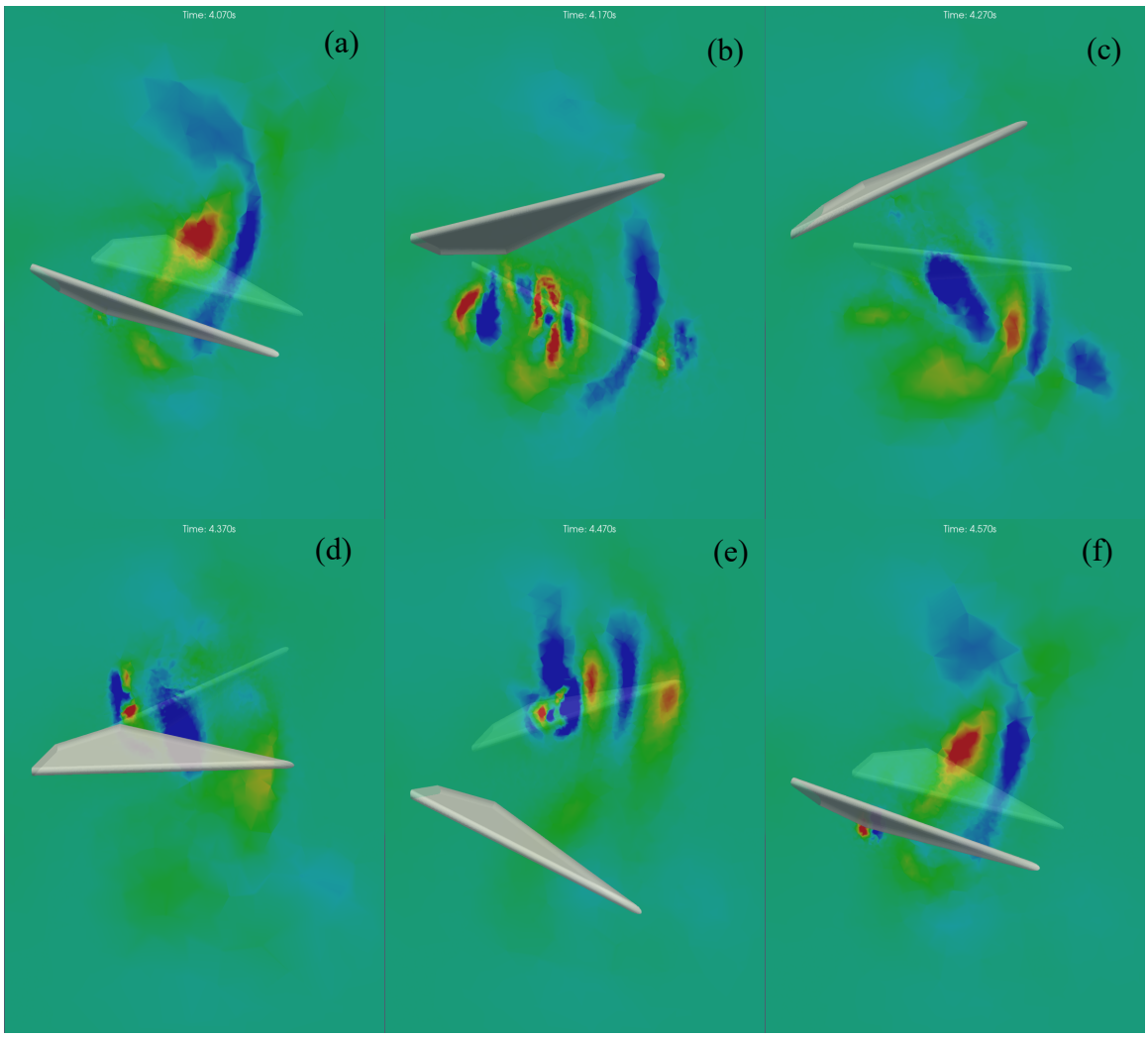


Fig. 38. Streamwise vorticity contours on a mid-plane between the tandem fins, *x*= 10.5cm, for the rigid fin, δ = -112.5°, at time (a) 4.07s, (b) 4.17s, (c) 4.27s, (d) 4.37s, (e) 4.47s and (f) 4.57s.

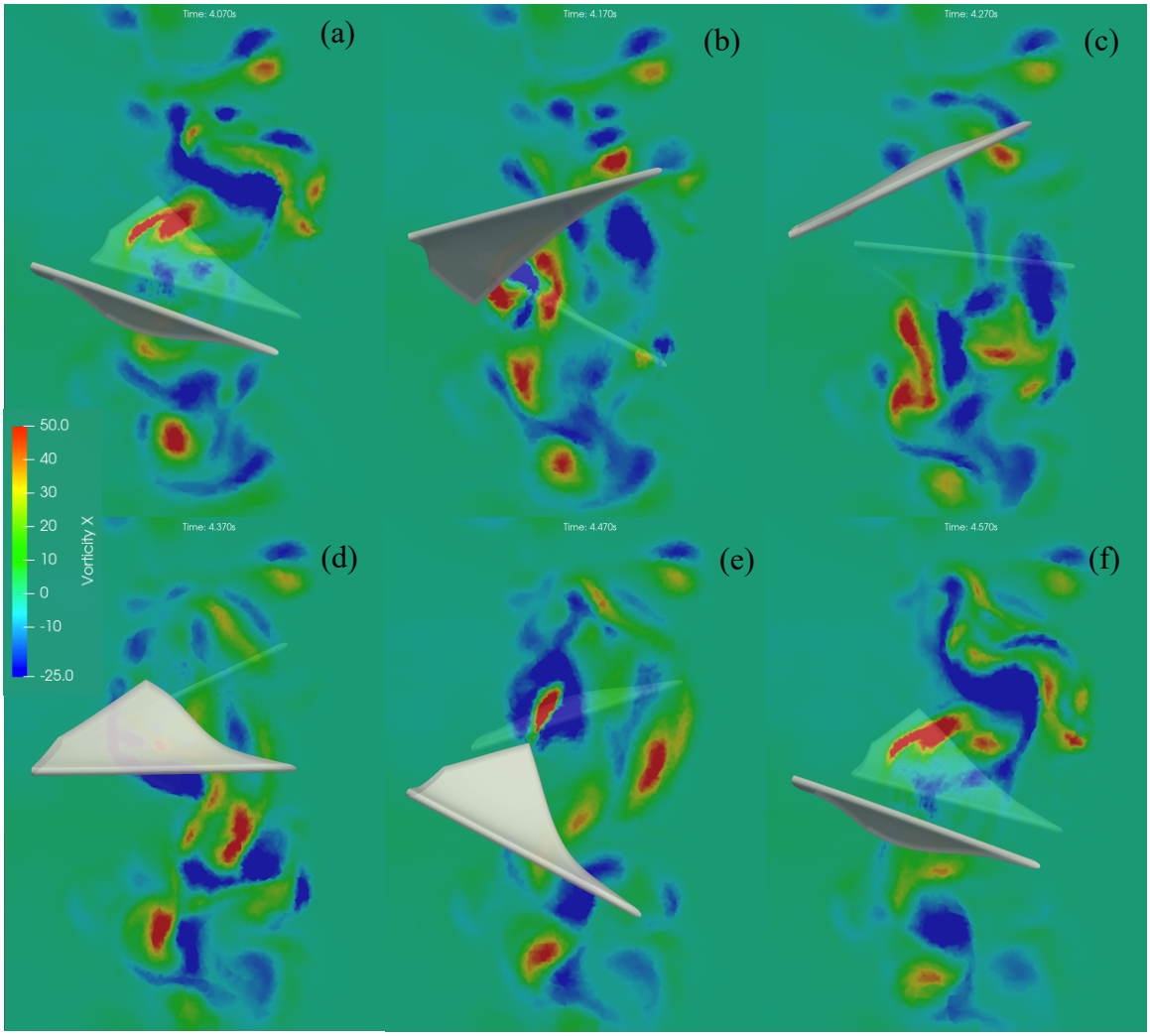


Fig. 39. Streamwise vorticity contours on a mid-plane between the tandem fins, $x$= 10.5cm, for the flexible fin E = 0.85MPa, δ = -112.5°, at time (a) 4.07s, (b) 4.17s, (c) 4.27s, (d) 4.37s, (e) 4.47s and (f) 4.57s.

evolution of the streamwise vorticity on a mid-plane between the two fins during one flapping cycle. At t= 4.17s, Fig. 38b, traces of several pairs of trailing edge vortices progressing in the spanwise direction can be seen. Some of these vortices interact with the leading edge of the rear fin to produce a maximum thrust at t= 4.27s, during the middle of its upstroke, and close to the middle of its downstroke at t=4.52s. Figures 39 and 40 show the vorticity evolution for the two flexible fins, and exhibit the production and merging of multiple vortex pairs. Again, as in the δ = 135° case, we can see the presence of the trailing edge vortices from the front fin in Fig. 39c, leading to a higher induced velocity and an increased thrust of the rear fin at t = 4.29s. For the more flexible fin with E = 0.31MPa, the vortices are much weaker and located below the leading edge of the rear fin, Fig. 40c, leading to a reduced thrust during the middle of the upstroke.

## SUMMARY AND FUTURE WORK

A CFD solver coupled with a structural solver using eigenmodes of the fin was used to simulate flexible flapping fin dynamics. In the current study, the coupled solver is used to simulate the force production from a pair of tandem flapping fins. Several parametric studies were

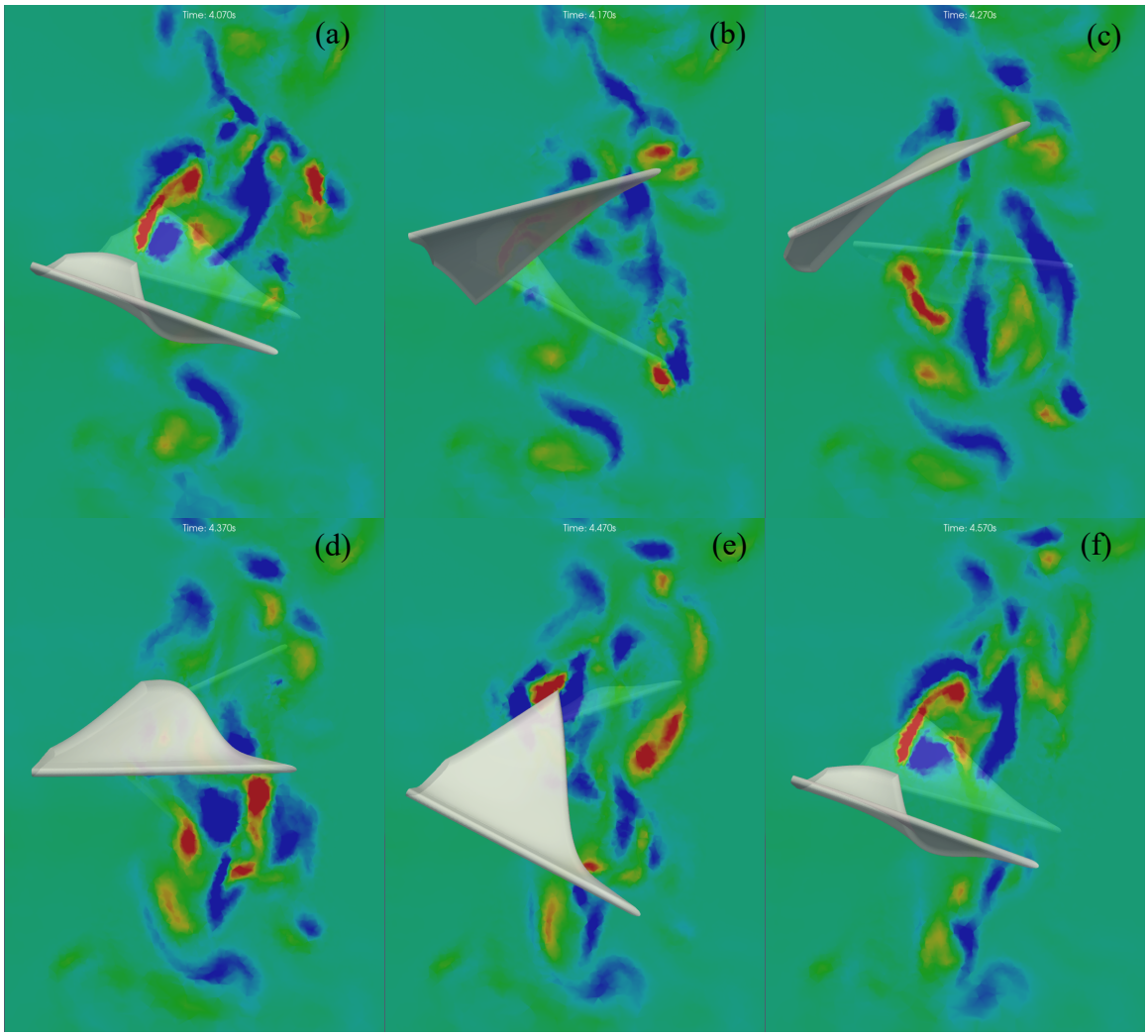


Fig. 40. Streamwise vorticity contours on a mid-plane between the tandem fins, $x$= 10.5cm, for the flexible fin E = 0.31MPa, δ = -112.5°, at time (a) 4.07s, (b) 4.17s, (c) 4.27s, (d) 4.37s, (e) 4.47s and (f) 4.57s.

performed varying the Young's moduli, the pitch amplitude, the flapping frequency of the fins, the axial offset and the phase offset between the front and the rear fins. Two flexible fins were considered and compared to its rigid counterpart. It was found that the flexible fin with E = 0.85MPa, performed better than the rigid fin. For all phase offsets considered, the rear fin of this set produced more thrust than the front fin, producing a maximum thrust when it lagged the forint fin by 135°, mainly due to the proper capture of the shed trailing edge vortex from the front fin. The more flexible fin, E = 0.31MPa, on the other hand produced less thrust than the rigid fin for the kinematics with a flapping frequency of 2Hz. The motion of the leading edge tip and trailing edge tips for all the flexible cases were monitored and shows that the more flexible fin produced nearly twice the trailing edge excursion of the more rigid fin. Velocity and vorticity data on several axial planes between and after the rear fin were collected for comparison with the experimental PIV results. The generated force data will provide a database for developing reduced order models for propulsive systems with flexible flapping fins.

**ACKNOWLEDGEMENTS**

This work was supported by NRL 6.2 base program on "Development of a Robust Onboard Control System for Bio-inspired UUVs." This work was performed by the first author when he was an employee at NRL and was supported in part by a grant of HPC time from the DoD HPC centers.

**REFERENCES**

1. Lauder, G.V., "Fish Locomotion: Recent Advances and New Directions," *Annual Review of Marine Science*, Vol. 7, pp. 521-545, 2015.
2. Kato, N., Ando, Y., Tomokazu, A., Suzuki, H., Suzomori, K., Kanda, T. and Endo, S., "Elastic pectoral fin actuators for biomimetic underwater vehicles", in Bio-mechanisms of Swimming and Flying, chap. 22, pp. 271-282, Springer Japan, 2008.
3. Wu, X., Zhang, X., Tian, X., Li, X., Lu, W., "A review on fluid dynamics of flapping foils. *Ocean Engineering*," Vol. 195, 106712, 2020.
4. Park, H., Park, Y.-J., Lee, B., Cho, K.-J., Choi, H., "Vortical structures around a flexible oscillating panel for maximum thrust in a quiescent fluid," *Journal of Fluids and Structures*. Vol. 67, pp. 241–260, 2016.
5. Sampath, K., Geder, J.D., Ramamurti, R., Pruessner, M.D., Koehler, R., "Hydrodynamics of tandem flapping pectoral fins with varying stroke phase offsets," *Physical Review Fluids*., Vol. 5, No. 9, 094101, 2020.
6. Li, Y., Xu, Y., Wu, Z., Ma, L., Guo, M., Li. Z., and Li, Y., "A Comprehensive Review on Fish-Inspired Robots," Intl. J. of Advanced Robotic Systems, May 2022.
7. Ramamurti, R., Geder, J., and Viswanath, K., "Coupled CFD and Structural Solver for Flapping Wing Simulations," NRL Technical Memorandum Report NRL/6041/MR--2022/3, Dec. 2022.
8. Ramamurti, R. and Löhner, R., "Evaluation of an Incompressible Flow Solver Based on Simple Elements," *Advances in Finite Element Analysis in Fluid Dynamics*, FED 137, Editors: Dhaubhadel, M. N. *et al*., ASME Publication, New York,1992, pp. 33-42.
9. Ramamurti, R., Löhner, R., and Sandberg, W. C., "Computation of the 3-D Unsteady Flow Past Deforming Geometries," *Int. J. Comp. Fluid Dyn.*, 13, 1999, pp. 83-99.
10. Turek, S., and Hron, J., "Proposal for Numerical Benchmarking of Fluid-Structure Interaction between an Elastic Object and a Laminar Incompressible Flow," *Fluid-Structure Interaction*, Springer Lecture Notes in Computational Science and Engineering, Vol. 53, Ed. H.-J. Bungartz & M. Schaefer, Springer Verlag 2006.
11. Ramamurti, R., Geder, J.D., Viswanath, K. and Pruessner, M., "Computational Fluid Dynamics Study of the Propulsive Characteristics of Tandem Flapping Fins, AIAA-2018-0039, AIAA Aerospace Sciences Meeting, Kissimmee, FL, January 2018.
12. Sampath, K., Xu, N., Geder, J.D., Pruessner, M., and Ramamurti, R., "Flapping Soft Fin Deformation Modeling using Planar Laser-Induced Fluorescence Imaging," *JoVE*, no. 182, p. 63784, Apr. 2022, doi: 10.3791/63784.
13. Sampath, K., Xu, N., Geder, J.D., Pruessner, M., and Ramamurti, R., "Wake Plane Analysis of Tandem Pectoral Fins with Stroke Phase Offsets,", in preparation, to be submitted to Phys. Review Letters, 2024.